

1 **A model of the methane cycle, permafrost, and hydrology of the Siberian**
2 **continental margin**

3 David Archer, University of Chicago

4 d-archer@uchicago.edu

5
6 **Abstract**

7 A two-dimensional model of a sediment column, with Darcy fluid flow,
8 biological and thermal methane production, and permafrost and methane
9 hydrate formation, is subjected to glacial / interglacial cycles in sea level,
10 alternately exposing the continental shelf to the cold atmosphere during
11 glacial times, and immersing in the ocean in interglacial times. The glacial
12 cycles are followed by a “long tail” 100-kyr timescale warming due to
13 fossil fuel combustion.

14 The salinity of the sediment column in the interior of the shelf can be
15 decreased hydrological forcing, to depths well below sea level, when the
16 sediment is exposed to the atmosphere. There is no analogous advective
17 seawater-injecting mechanism upon resubmergence, only slower diffusive
18 mechanisms. This hydrological ratchet is consistent with the existence of
19 fresh water beneath the sea floor on continental shelves around the
20 world, left over from the last glacial time.

21 The salt content of the sediment column affects the relative proportions
22 of the solid and fluid H₂O-containing phases, but in the permafrost zone
23 the salinity in the pore fluid brine is a function of temperature only,
24 controlled by equilibrium with ice. Ice can tolerate a higher salinity in the
25 pore fluid than methane hydrate can at low pressure and temperature,
26 excluding methane hydrate from thermodynamic stability in the
27 permafrost zone. The implication is that any methane hydrate existing
28 today will be insulated from anthropogenic climate change by hundreds of
29 meters of sediment, resulting in a response time of thousands of years.

30 The strongest impact of the glacial / interglacial cycles on the
31 atmospheric methane flux is due to bubbles dissolving in the ocean when
32 sea level is high. When sea level is low and the sediment surface is
33 exposed to the atmosphere, the atmospheric flux is sensitive to whether
34 permafrost inhibits bubble migration in the model. If it does, the

35 atmospheric flux is highest during the glaciating, sea-level regression (soil
36 freezing) part of the cycle, rather than during deglacial transgression
37 (warming and thawing).

38 The atmospheric flux response to a warming climate is small, relative to
39 the rest of the methane sources to the atmosphere in the global budget,
40 because of the ongoing flooding of the continental shelf. The increased
41 methane flux due to ocean warming could be completely counteracted by
42 sea level rise of tens of meters on millennial time scales due to loss of ice
43 sheets, decreasing the efficiency of bubble transit through the water
44 column. The model results give no indication of a mechanism by which
45 methane emissions from the Siberian continental shelf could have a
46 significant impact on the near-term evolution of Earth's climate, but on
47 millennial timescales the release of carbon from hydrate and permafrost
48 could contribute significantly to the fossil fuel carbon burden in the
49 atmosphere / ocean / terrestrial carbon cycle.

50 **1. Introduction**

51 ***1.1 The Siberian Continental Shelf System***

52 The Siberian Arctic continental shelf has been the focus of attention from
53 scientists and the public at large for its potential to release methane, a
54 greenhouse gas, in response to climate warming, a potential amplifying
55 positive feedback to climate change [*Shakhova, 2010; Westbrook,*
56 *2009*]. The goal of this paper is to simulate the geophysical and carbon
57 cycle dynamics of the Siberian continental margin within the context of a
58 basin- and geologic time-scale mechanistic model of the coastal margin
59 carbon cycle called SpongeBOB [*Archer et al., 2012*]. An initial condition
60 for the glacial cycle simulations was generated by spinning the model up
61 at low resolution over 62 million simulated years. Then the model at
62 higher resolution is driven by cyclic changes in sea level and air
63 temperature resulting from glacial cycles, to simulate the impact of the
64 hydrological pressure head and permafrost formation on the fluid flow and
65 methane cycle on the shelf. Finally, an 100,000-year interglacial interval
66 in the simulation is subjected to anthropogenic warming of the overlying
67 water and potential 60-meter changes sea level. Sensitivity studies are
68 presented for the biogenic and thermogenic methane production rates,
69 initial salinity, geothermal temperature gradient, rates of hydrological
70 flow, and permafrost impact on gas mobility.

71

1.1.1 Permafrost

72 One component of the simulation is a wedge of frozen sediment
73 (permafrost) submerged beneath the ocean on the continental shelf of
74 Siberia, left behind from glacial time when the shelves were exposed to
75 the frigid atmosphere by lowered sea level [*Romanovskii and Hubberten,*
76 2001]. The ice is thought to provide a seal to upward migration of
77 methane gas [*Shakhova et al., 2009*], especially where ancient fresh
78 groundwater flow produced a layer of very high saturation ice infill, a
79 formation called the Ice Complex in Siberia [*Romanovskii et al., 2000*],
80 although there are high ice saturations found in the Alaskan Arctic as well
81 [*Zimov et al., 2006*].

82 With inundation by the natural sea level rise over the last 10+ thousand
83 years, the permafrost is transiently melting, although the time constant
84 for this is generally long enough that significant frozen volume remains,
85 especially in shallower waters which were flooded more recently
86 [*Khvorostyanov et al., 2008a; Nicolovsky and Shakhova, 2010; Romanovskii*
87 *and Hubberten, 2001; Romanovskii et al., 2004; Shakhova et al., 2009;*
88 *Taylor et al., 1996*]. Even overlying water at the freezing temperature
89 can provoke subsurface melting by providing a warmer boundary
90 condition against which geothermal heat establishes the subsurface
91 temperature profile, but with climate warming, the waters could surpass
92 the freezing temperature, allowing heat to flow from above as well as
93 below [*Khvorostyanov et al., 2008b*].

94 Elevated methane concentrations have been measured in the water
95 column over the Siberian shelf, even in areas of shallow water where the
96 permafrost should still be strongly intact [*Shakhova, 2010; Shakhova et*
97 *al., 2005*]. Chemical and isotopic signatures of hydrocarbons adsorbed
98 onto surface sediments indicate a thermal origin [*Cramer and Franke,*
99 2005], suggesting that the methane is produced many kilometers deep in
100 the sediment column. The apparent ability for this methane to transverse
101 the barrier of the Ice Complex has been attributed to hypothesized
102 openings in the ice (called “taliks”), resulting from lakes or rivers on the
103 exposed shelf, or geologic faults [*Nicolovsky and Shakhova, 2010;*
104 *Romanovskii et al., 2004; Shakhova et al., 2009*].

105

1.1.2 Salt

106 Dissolved salt in the pore waters can impact the timing of thawing
107 permafrost [*Nicol'sky and Shakhova, 2010; Shakhova et al., 2009*]. When
108 sea level drops and exposes the top of the sediment column to the
109 atmosphere and fresh water, the salinity of the subsurface pore waters
110 can be flushed out by hydrological groundwater flow, driven by the
111 pressure head from the elevated terrestrial water table above sea level.
112 The boundary between fresh and salty pore water tends to intersect the
113 sediment surface at the water's edge [*Moore et al., 2011*]. From there,
114 the boundary tends to dip landward, to a depth of approximately 40
115 meters below sea level for every 1 meter of elevation of the table water.
116 The ratio of water table elevation to freshwater lens depth is driven by
117 the relative densities of fresh and salt water, as the fluid seeks an
118 isostatic balance in which the fresh water displaces an equal mass of salt
119 water [*Verrjuit, 1968*].

120 The SpongeBOB model has been modified to simulate the processes
121 responsible for these observations. We do not attempt to simulate a
122 detailed outcropping history over 62 million-year spinup time of the
123 sediment column, but rather demonstrate the general process by
124 subjecting the nearly complete sediment column to a one-time sea level
125 lowering, exposing the continental shelf to groundwater forcing (see
126 [Supplemental Text S4](#)). After a few million years, the sediment column
127 subsides, due to compaction and absence of sediment deposition,
128 resulting in a sediment column that has been considerably freshened by
129 the atmospheric exposure. This freshening persists in the model for
130 millions of years, because there is no corresponding "salt-water pump"
131 during high sea-level stands. This behavior is consistent with the
132 discovery of vast nearly fresh aquifers in currently submerged continental
133 shelf regions around the world [*Post et al., 2013*], left over from
134 groundwater forcing during glacial time.

135

1.1.3 Carbon

136 Another component of the simulation is the Yedoma, deposits of wind-
137 blown dust and organic carbon that accumulated on the coastal plains of
138 exposed continental shelves during glacial times [*Zimov et al., 2006*].
139 The deposits contain a substantial fraction of organic carbon, consisting
140 of grass roots and remains, preserved by the freezing conditions. When
141 they thaw, they begin to release CO₂ and methane to the atmosphere

142 [Dutta et al., 2006; Schuur et al., 2008; Zimov et al., 2006]. Oxidation
143 of the carbon can give off enough heat to accelerate the melting driven
144 by primary climate forcing [Khvorostyanov et al., 2008b].

145 **1.2 Models of Methane Hydrate in the Permafrost Zone**

146 The dynamics of the permafrost layer, and its present state, have been
147 extensively modeled within detailed maps of the crust and sediment
148 structure [Gavrilov et al., 2003; Nicolsky and Shakhova, 2010; Nicolsky et
149 al., 2012; Romanovskii and Hubberten, 2001; Romanovskii et al., 2005].
150 Methane hydrate modeling has been done in the Arctic applied to the
151 Siberian continental slope [Reagan, 2008; Reagan and Moridis, 2009;
152 Reagan et al., 2011], but only one calculation has been done in the
153 context of permafrost formation [Romanovskii et al., 2005], as found on
154 the shelf. Romanovski [2005] modeled the extent of the methane
155 hydrate stability zone through glacial cycles, but based the calculations
156 on marine salinity values when calculating the stability of hydrate. I will
157 argue that in sub-freezing conditions (in the permafrost zone) the only
158 water available for hydrate formation will be in a saline brine that would
159 be in equilibrium with ice at the local temperature. This formulation
160 restricts hydrate stability from the permafrost zone to greater depth
161 below the sea floor than if the salinity was unaffected by formation of ice.

162 **1.3 Outline of This Work**

163 The model description in Section 2 begins with a description of the
164 previously published aspects of the SpongeBOB model as it is applied to
165 the Siberian margin (2.1). New developments in the code include
166 pressure-head driven groundwater flow (2.2), permafrost formation and
167 its impacts on the thermodynamics of ice and hydrate (2.3), and the
168 calculation of the methane flux to the atmosphere (2.4). The procedure
169 for generating the initial condition sediment column for the glacial /
170 interglacial cycles (2.5) is presented along with a description of the
171 forcings imposed to generate the glacial / interglacial cycles (2.6), and
172 the subsequent anthropocene (2.7). The formulation and rationale for
173 the sensitivity studies is given in Section 2.8.

174 The Results in Section 3 include a discussion of the model behavior
175 through the glacial / interglacial cycles (3.1), and in response to
176 anthropogenic global warming scenarios (3.2). A summary of model

177 sensitivity study results is given in Section 3.3, and comparison with field
178 observations in Section 3.4.

179 The Discussion in Section 4 includes the model limitations and critical
180 issues for future development (4.1), followed by the robust features of
181 the model simulations (4.2).

182 **2. Model Description**

183 ***2.1 SpongeBOB Application to the Siberian Continental Margin***

184 SpongeBOB is a two-dimensional basin spatial-scale and geological time-
185 scale model for the methane cycle in continental margin sediments. The
186 model, configured for a passive margin basin, was described by Archer et
187 al [2012], applied to the Atlantic coast of the United States. The
188 bottom boundary is bedrock, and accumulation time scales are millions of
189 years, as sediment is introduced as coastal riverine material, and settles
190 on the sea floor. Isostatic adjustment and crustal subsidence make room
191 for the accumulation of 5-10 km of sediment, which progrades seaward in
192 sigmoidal packages, driven by a maximum sediment accumulation rates
193 just off the shelf break.

194 Here the model framework is used as a representation of the continental
195 shelf of Siberia, although the tectonic and depositional histories of the
196 region are heavily impacted by vertical tectonic motions not represented
197 in the model. The crust underlying the continental shelf area has been
198 alternately rising and subsiding in blocks called horsts and grabens
199 [Nicol'sky et al., 2012]. The sediment cover on the grabens is thick much
200 thicker than it is in the horsts, thick enough for thermal methane
201 production. The thickness of the sediment cover in the model ranges
202 from 5 – 10 kilometers throughout the domain, reminiscent of the
203 grabens (subsiding blocks), because thermogenic methane is an essential
204 part of the simulations.

205 The model maintains a concentration of particulate organic carbon, with
206 which it predicts rates of methanogenesis. However, because the
207 depositional histories and organic carbon concentrations in the Siberian
208 continental margin are not well constrained, the rates of biological and
209 thermal methane production predicted by the model are unreliable
210 predictors of reality. For this reason, methanogenesis rates in the model
211 are scaled arbitrarily as tunable model inputs. The depth distributions of

212 the sources depend mostly on temperature, an easier variable to predict
 213 than organic carbon degradation activity.

214 **2.2 New Model Development: Groundwater Hydrology**

215 **2.2.1 Pressure Head**

216 When the sediment column is exposed to the atmosphere, the pressure
 217 field from the variable elevation of the water table (the pressure head)
 218 begins to affect the fluid flow. The pressure head for a fluid particle at
 219 the depth of the water table varies as

$$220 \quad P_{\text{head}}(z) = g \int_z^{z_{\text{wt}}} \rho_{\text{fluid}} dz$$

221 where z_{wt} is the elevation of the water table, which affects the pressure
 222 throughout the fluid column, and the integral of the fluid density allows
 223 the pressure at depth to be affected by the salinity and temperature of
 224 the water above. The depth of the water table is a prognostic variable in
 225 the model. In these simulations, however, the water table remains very
 226 close to the sediment surface, as unsaturated soil produced by
 227 subsurface flow is quickly replenished by hydrological recharge.

228 **2.2.2 Pore Fluid Flow**

229 The pressure head acts in concert with the excess pressure P_{excess} , as
 230 defined by Archer et al. [2012], to drive horizontal Darcy flow through
 231 the sediment. The value of P_{excess} is determined from the porosity and
 232 sediment load of the sediment in each grid box. An assumed sediment
 233 rheology is used to calculate the load-bearing capacity of the solid matrix
 234 within a given grid cell. P_{excess} is calculated by assuming that the load of
 235 the solid phase overlying the grid cell that is not carried by the solid
 236 matrix must be carried by the P_{excess} in the fluid phase.

237 The horizontal flow is

$$238 \quad u_{\text{Darcy},i \rightarrow i+1} = \frac{k_{h,i} + k_{h,i+1}}{2\mu} \frac{(P_{\text{excess},i} - P_{\text{excess},i+1}) + (P_{\text{head},i} - P_{\text{head},i+1})}{(\Delta x_i + \Delta x_{i+1})/2}$$

239 while the vertical flow in the model is driven only by compaction pressure

$$240 \quad w_{\text{Darcy},j \rightarrow j+1} = \frac{k_{v,j}}{\mu} \frac{P_{\text{excess},j} - P_{\text{excess},j+1}}{(\Delta z_j + \Delta z_{j+1})/2}$$

241 where $k_{h,i}$ is the horizontal permeability at horizontal cell index j , $k_{v,j}$ is
242 vertical permeability at vertical index j , μ is the viscosity, and Δx and Δz
243 are cell dimensions. Notes on numerical issues are given in [Supplemental](#)
244 [Text S1](#).

245 **2.2.3 Canyons**

246 The model as described so far represents a laterally homogeneous slab, a
247 poor approximation for hydrology above sea level because of the
248 formation of canyons and river networks in a real drained plateau. The
249 depth of the water table in a river canyon is depressed, relative to the
250 surroundings, to the depth of the canyon. The water table is higher in
251 between the canyons because of recharge, and the difference in head
252 drives lateral flow, the canyons acting to drain the sediment column.

253 The model formulation has been altered to represent this mechanics in a
254 simplified way. Rather than expand the model into the full third
255 dimension, the 2-D field of the model is held to represent the sediment
256 column at a hypothetical ridge crest, as altered by an adjacent canyon.
257 The canyon elevation is represented by z_{canyon} , and its width by a scale
258 Δy_{canyon} . A cross-column flow velocity $v_{\text{Darcy},j}$ is calculated as

$$259 \quad v_{\text{Darcy},j} = \frac{k_{h,j} (P_{\text{head,canyon}} - P_{\text{head}})}{\mu \Delta y_{\text{canyon}}}$$

260 where $P_{\text{head,canyon}}$ is the pressure head as a function of depth in the
261 hypothetical canyon, calculated assuming that the water table outcrops
262 at z_{canyon} , and that the temperatures in the sediment column have
263 adjusted to the formation of the canyon, such that the near-surface
264 geothermal gradient is the same between the hypothetical canyon and
265 the bulk sediment column. The lateral “drainage” flow ($v_{\text{Darcy},j}$) drives
266 vertical velocities by continuity.

267 The horizontal distance scale Δy_{canyon} is somewhat arbitrary and difficult to
268 constrain, given that in the reality of river networks the distance to the
269 nearest canyon from any point in the domain is likely to be a function of
270 altitude, distance from the coast, and time. Another poorly resolved
271 factor is the depth of the canyon. In reality, canyons cut into a plateau
272 following a dynamic that erosion is proportional to slope, stopping at sea
273 level. As a simplification the model is set to hold the canyon depth at
274 current sea level throughout the simulation.

275 In the real fractal geometry of canyons, the spacing between canyons
276 across a plain is similar to the width of the plain (length of the canyons),
277 so the Base simulation assumes a canyon width of 100 km, based on the
278 100+ km width scale of the continental shelf.

279 **2.3 Permafrost**

280 **2.3.1 Thermodynamics of Ice and Hydrate**

281 The ice model is based on an assumption of thermodynamic equilibrium, in
282 which the heat content of the cell is distributed between the pure ice,
283 hydrate, and brine phases, while the salt content is restricted to the
284 brine. Notes on numerical implementation are given in [Supplemental Text](#)
285 [S2](#).

286 In the permafrost zone where ice is present, the salinity of the brine
287 creates an ice-freezing point depression that matches the local
288 temperature. This equilibrium salinity is higher than methane hydrate can
289 tolerate, excluding hydrate from thermodynamic stability. For a more
290 detailed examination of the role of the brine salinity in determining the
291 relative stabilities of ice and hydrate, see [Supplemental Text S3](#).

292 **2.3.3 Other Impacts**

293 Permafrost formation has several impacts on the methane cycle in the
294 model. Biogenic methanogenesis is assumed stopped in the ice fraction
295 of a grid cell (which approaches unity but never reaches it in the model,
296 due to exclusion of salt into brine). Bubble transport in the model
297 balances bubble production, driven by a small and not very well
298 constrained standing bubble concentration within the pore space. It is
299 generally assumed [*Shakhova et al.*, 2010b] that permafrost inhibits gas
300 transport through the sediment column, both based on sediment column
301 carbon and hydrogen budgets [*Hunt*, 1995] and on the tight seal
302 provided by the ice complex. The seal provided to Arctic lakes, which can
303 drain overnight if the seal is breached, also lends credence to this idea. In
304 the model, this effect was simulated by stopping gas transport
305 completely when a grid cell exceeds 50% ice fraction (with sensitivity
306 runs assuming 10%, 30%, 70%, and 90%).

307 **2.4 Atmospheric Methane Fluxes**

308 Bubbles emerging from the sediment column into the water column of the
309 ocean may dissolve in the water column, or they may reach the sea
310 surface, a direct methane flux to the atmosphere [*Westbrook et al.*,
311 2009]. In the model, bubble dissolution in the water column is assumed
312 to attenuate the bubble flux according to the water depth with an e-
313 folding attenuation scale of 30 meters [*Gentz et al.*, 2014; *Portnov et al.*,
314 2013; *Westbrook et al.*, 2009]. In reality, a low-flux gas seep, producing
315 small bubbles, will probably not reach as far into the water column as a
316 30-meter scale height, while a faster seep can reach further. Methane
317 dissolved in the water column, in reality, may survive oxidation (time
318 constant of about a year), and degas to the atmosphere, but this
319 possibility is not included in the model. For land grid points (exposed to
320 the atmosphere by lowered sea level), any upward bubble flux at the
321 sediment surface is assumed 100% released to the atmosphere. The
322 model neglects methane oxidation in soils, as well as many other
323 terrestrial processes such as thaw bulbs beneath bodies of water [*Walter*
324 *et al.*, 2006], and the seasonal cycle of melting and thawing in the
325 surface active layer. See discussion in [Section 4.1](#).

326 **2.5 Initial Condition**

327 **2.5.1 Rational for Spinup**

328 The point of the spinup phase is to generate an initial condition for the
329 glacial cycle simulations. The more usual approach in modeling hydrates
330 is to start with an ad-hoc initial condition [*Reagan*, 2008; *Reagan and*
331 *Moridis*, 2009; *Reagan et al.*, 2011]. For SpongeBOB the model state at
332 any time is the result of the time-history of sedimentation, which is driven
333 by the time-evolving depth of the sea floor, and interacting with isostatic
334 adjustment of the crust. The simplest way to generate an initial condition
335 in the model without a startup transient is to spin the model up from
336 bedrock. The duration of the spinup phase is 62 million years, roughly
337 consistent with the time scale since the opening of the Laptev Rift. The
338 first 60 Myr used a relatively coarse resolution as shown in [Figure 1a](#). For
339 the glacial / interglacial experiments, the initial condition was interpolated
340 to a higher resolution grid in the vertical, as shown in [Figure 1b](#).

341

2.5.2 Sediment Column Salt Content

342 When sea level drops such that the surface of the sediment column
343 outcrops to the atmosphere, the pore fluid becomes subject to the
344 pressure head driving it seaward, and to fresh water recharge from
345 precipitation. The pressure head forcing and the buoyancy of the
346 sediment fluid column combine to create a mechanism to excavate
347 salinity from the upper sediment column, to depths well below sea level.
348 The salinity of the sediment column tends to be ratcheted down by
349 exposure to the atmosphere, because there is no comparable advective
350 pump for reinvasion of seawater when sea level rises.

351 A “pre-freshened” sediment column was constructed by dropping sea
352 level by 120 meters and holding it there for millions of years. The
353 sediment column subsides back into the ocean over a few million years,
354 but the fresh imprint of the hydrological flow persist for millions of years
355 (Figure 2a and Supplemental Text S4). If the sediment surface never
356 outcrops, the pore salinities remain nearly uniform and marine (Figure 2b).
357 Particulate organic carbon (POC) concentrations are highest just off the
358 shelf break (Figure 3), because this is where most of the sediment is
359 deposited, and because the sedimentary material is richest in POC in
360 shallow ocean water depths [Archer *et al.*, 2012]. Methane concentration
361 (Figure 4a) closely mirrors the solubility of dissolved methane, resulting in
362 near saturation concentrations through most of the model domain (Figure
363 4b). The pre-freshened (Fr) versus marine (Mr) initial conditions are
364 taken as end member salinity sensitivity runs (see Table 1).

365 2.6 Glacial Cycle Forcing

366 Beginning from an entirely submerged initial condition, the model is
367 subjected to 100-kyr sawtooth cycles of sea level ranging between -120
368 to +20 meters from the initial sea level (starting at -120 for
369 prefreshened, 0 for pure marine) (Figure 5a). The model forcing scenarios
370 are summarized in Table 1.

371

2.6.1 Sea Level

372 The simplest scenario (SL) varies the sea level while keeping the air and
373 water temperatures time-invariant. The sea-level air temperature is
374 maintained at 0 °C. This simulation is nearly permafrost-free, with a small
375 exception where the altitude of the sediment surface is much higher than

376 sea level (due to the lapse rate in the atmosphere). There is no
377 deposition of sediment above sea level in this simulation.

378 **2.6.2 Glacial Climate**

379 Permafrost formation is added in simulation GL, in which the air
380 temperature ramps down to -16 °C at sea level, linearly with the glacial
381 sea level fall (Figure 5b). In the ocean, shelf waters are always -1.8 °C,
382 but an interglacial subsurface temperature maximum of 1 °C at 200
383 meters decreases to -1.8 °C during glacial times.

384 **2.6.3 Deposition of Carbon on Land**

385 Deposition of organic-rich sediments when the surface is exposed to the
386 atmosphere (Yedoma: represented as accumulation of 10 meters in 100
387 kyr, with 30% POC) is added in scenarios SL+LD and GL+LD (LD for land
388 deposition).

389 **2.7 Anthropogenic Global Warming Forcing**

390 **2.7.1 Long-Term Climate Impact from CO₂ Addition**

391 The global warming (GW) scenario begins from a high sea-level interglacial
392 state, and raising the temperature following the climate impact of the
393 “spike and long tail” time distribution of a slug of new CO₂ added to the
394 atmosphere [Archer *et al.*, 2009] (Figure 8). There is a stage of fast
395 atmospheric drawdown as CO₂ invades the ocean, but once the ocean,
396 atmosphere, and land surface reach equilibrium (after a few hundred
397 years), the CO₂ content of the entire biosphere begins to relax toward an
398 initial “natural” value, on time scales of hundreds of thousands of years,
399 by weathering reactions with carbonate and siliceous solid rocks. The net
400 result is a CO₂ drawdown that can be expressed as the sum of several
401 exponential functions in time, with time scales ranging from 10² – 10⁶
402 years.

403 Changes in water column temperature are assumed equal to those of the
404 atmosphere, following paleoceanographic reconstructions [Martin *et al.*,
405 2002] and long-term coupled ocean / atmosphere circulation model
406 experiments [Stouffer and Manabe, 2003]. The GW scenario imposes this
407 temperature change on the water column, relaxing toward equilibrium
408 with the atmospheric CO₂ trajectory with a time constant of 100 years.

409

2.7.2 Long-Term Behavior of Sea Level

410 The effect of sea level rise is added to create a second global warming
411 scenario GW+SL. On time scales of thousands of years the sea level
412 response to changing global temperature is much stronger than the sea
413 level response over the coming century, as prominently forecast by the
414 IPCC. Reconstruction of sea level and global temperature covariation in
415 the geologic past (glacial time to Eocene hothouse) reveals a covariation
416 of 10-20 meters per °C [Archer and Brovkin, 2008]. The global warming
417 with sea level scenario assumes an equilibrium sea level response of 15
418 meters / °C, which it relaxes toward with a time constant of 1000 years.

419 **2.8 Sensitivity Studies**

420 A strategy for dealing with the many uncertainties in the model
421 formulation and parameterization is to do sensitivity studies, to
422 determine which of the unknowns are most significant. The model
423 sensitivity studies are summarized in [Table 1](#). Sensitivity studies to the
424 rates of methane production have already been mentioned, as have the
425 pre-freshened versus marine initial conditions, representing uncertainty in
426 the salt content of the sediment column. Other model sensitivity runs
427 include the geothermal temperature gradient, and a parameterization of
428 permafrost inhibition of bubble migration. Several altered-physics runs
429 were done, one adding vertical permeable channels, one disabling
430 horizontal flow, and several to evaluate the impact of ice formation on
431 methane hydrate stability.

432 **3. Results**

433 **3.1 Glacial Cycles**

434

3.1.1 Salinity

435 In the “prefreshened” initial condition (Fr), millions of years have elapsed
436 since the previous exposure of the sediment to hydrological forcing, but a
437 core of fresh water remains. Salinities near the sediment surface have
438 grown saltier due to diffusive contact with seawater ([Figure 6, left](#)). A
439 fully marine initial condition (Mar) ([Figure 6, right](#)) was initialized from the
440 unfreshened case, in which sea level was held at a fixed value throughout
441 the 65 Myr spinup of the sediment column. The salinities are nearly
442 uniform in this case.

443 When the sediment surface is re-exposed to the atmosphere during an
444 interval of low sea level, in the absence of ice formation (simulation SL),
445 the surface layer tends to freshen relatively quickly due to the
446 hydrological forcing, although a subsurface salinity maximum persists
447 (Figure 6c and d). If the air temperatures are cold enough to form ice
448 (simulation GL), surface salinities in the model increase to up to nearly
449 190 psu, in both prefreshened and pure marine cases (Figure 6e and f).
450 By the next interglacial time (Figure 6g and h), ice near the sediment
451 surface has melted enough for near-surface pore waters to reach
452 relatively low salinities.

453

3.1.2 Pressure and Flow

454 The effect of the glacial / interglacial sea level and climate forcing on the
455 pressures and flow velocities are shown in Figure 7. On a spatial scale of
456 the entire model domain (Figure 7, left), the highest driving pressures are
457 found at the base of the sediment column, underneath the region of
458 maximum sediment accumulation (the depocenter just off the shelf
459 break). Changes in sea level drive large fluctuations in the pressure head
460 (contours) extending to bedrock. In the near-surface continental shelf
461 (Figure 7, right), the driving pressure variations are dominated by the
462 pressure head, driven by sea level changes. The formation of permafrost
463 (GL, Figure 7 e and f) seals the upper sediment column to fluid flow.

464 When sea level rises again, in the model configuration including
465 permafrost, there is a strong pulse of downward flow following partial
466 melting of the permafrost (Figure 7 h). It is possible that this flow, which
467 lasts a few thousand years, is an artifact of the elastic model
468 configuration, in which the release of a load (by submergence of the
469 upper sediment column into the ocean) provokes the expansion of pore
470 spaces in the sediment. The anomalous flow, integrated over its duration,
471 could displace the pore fluid by about 40 meters, which is less than one
472 grid cell. The model configuration without the sealing effect of permafrost
473 (SL) does not show this pulse of invasive flow on sea level rise.

474

3.1.3 Methane Cycle

475 There are multiple ways in which the glacial cycles of sea level and air and
476 water temperature might impact the flux of methane to the atmosphere.
477 Submergence in the ocean is one modulating factor, because the
478 emerging bubbles dissolve in the ocean rather than reaching the

479 atmosphere. Another factor is the deposition of high-POC surface soils
480 during low sea level stands, and its exposure to degradation later when
481 the permafrost soils melt. A third factor is permafrost, impeding gas and
482 fluid flow and excluding dissolved methane and salt from ice formation.
483 The impacts of these processes are assessed by comparing the results
484 from model configurations with and without each process in question.

485 **Ice vs. Hydrate.** The impact of phase competition between ice and
486 hydrate is shown in [Figure 8](#). In the Base scenario ([Figure 8a and c](#))
487 hydrate stability is excluded from the permafrost zone as described in
488 [Supplemental Text S3](#). Preventing ice from forming in an altered-physics
489 simulation (+ No Ice) decreases the fluid-phase salinity relative to the
490 Base simulation, and allows the methane hydrate stability zone to nearly
491 reach the sea floor ([Figure 8b and d](#)), during strongest glacial conditions.
492 Another altered-physics simulation was done in which ice is allowed to
493 form, but not affect the salinity as it drives methane hydrate stability
494 (which was hard-wired to marine salinity). Methane hydrate is still
495 unstable in the permafrost zone through most of the simulation (see
496 movie files in supplemental material), indicating that thermal interaction
497 must also have a strong impact on methane hydrate stability in the
498 permafrost zone.

499 **Dissolved Methane.** The evolution of the dissolved methane
500 disequilibrium condition ($\text{CH}_4 / \text{CH}_{4 \text{ sat}}$) is shown in [Figure 9](#). At the
501 initiation of the glacial cycles, methane is undersaturated in near-surface
502 sediments on the continental shelf, by diffusive contact with the
503 methane-free ocean upper boundary condition. In the prefreshened
504 sediment column scenario (Fr), methane concentrations in the depth
505 range of 100-1000 meters are lower than in the marine case (Mar, [Figure](#)
506 [9b](#)), due to the ventilation by the hydrological pump ([Figure 9a](#)). Further
507 freshening of the pore waters in the ice-free case (SL+LD) tends to
508 deplete methane in the upper sediment column ([Figure 9c-e](#)), while
509 methane exclusion from the permafrost ice leads to supersaturation in
510 simulation GL+LD ([Figure 9f-h](#)). The hydrate stability zone is somewhat
511 expanded in the prefreshened sediment column relative to the marine
512 case ([Figure 9 g vs. h, heavy black contour](#)).

513 **Methane Sources.** [Figure 10](#) shows snapshot sections of various
514 aspects of the shelf carbon cycle, beginning from a prefreshened initial
515 condition. Sections of POC concentration in [Figure 10, left](#) show the
516 accumulation of POC-rich Yedoma deposits on land ([Figure 10 g and j](#)).

517 The rate of methane production in the model (Figure 10, right) depends
518 on temperature and organic carbon age, but it is also attenuated by
519 permafrost formation in the model, scaling to zero in the completely
520 frozen case. Methanogenesis rates are near zero in the permafrost zone
521 during glacial time (Figure 10h), but partially recover during interglacial
522 time (Figure 10k) even though permafrost is still present.

523 **Hydrate.** A zone of methane hydrate stability exists below the
524 permafrost zone when permafrost is present, and some methane hydrate
525 accumulates in that zone. The highest pore-fraction values are found
526 near the continental slope, where the shelf stability field outcrops within
527 the slope depocenter. Dissolved methane concentrations exceed
528 saturation within the stability zone in the model (Figure 9), but the
529 accumulation of methane hydrate (Figure 10, right) is limited by the rate
530 of methane production.

531 Time series plots of the inventory of methane as hydrate on the shelf are
532 shown in Figure 11. The integration cuts off at $x=560$ km to exclude the
533 sediment depocenter on the continental slope. Hydrate inventories reach
534 maximum values during deglaciations. There is more hydrate when the
535 pore water is fresher, and there would be more if ice were excluded from
536 forming (Figure 11a). The hydrate inventory is much more sensitive to
537 thermogenic methane production, deep in the sediment column, than
538 Yedoma deposition (Figure 11b). The impact of the geothermal heat flux
539 is to change the depth of the bottom of the hydrate stability zone
540 (Figure 18 e and f), but the impact is small on the hydrate inventory,
541 unless the temperature gradient is so low that hydrate persists through
542 the entire glacial cycle (Figure 11c). The hydrate forms from the
543 dissolved methane pool, which exceeds 1000 Gton C in shelf porewaters
544 of the model.

545 **Permafrost, Ocean, and Atmospheric Methane Flux.** The impact
546 of the glacial cycles on the methane pathway to the atmosphere in the
547 model is shown in Figure 12. When sea level is high, the efficiency of
548 bubble transport across the sediment-water interface reaching the
549 atmosphere ranges from about 75% near the coast to about 10% at the
550 shelf break (Figure 12a). Most of the methane flux from the sediment is
551 located just off the shelf break (Figure 12e), where the escape efficiency
552 is low, so not much methane makes it to the atmosphere during the
553 interglacial. During glacial times, the sediment column is exposed to the
554 atmosphere, and the escape efficiency in the model is 100% (Figure

555 12b). Permafrost inhibits the terrestrial methane flux (Figure 12i)
556 relative to the case without permafrost (Figure 12f). During some
557 deglaciations, the release of pent-up gas by permafrost degradation leads
558 to a spike of excess methane flux to the atmosphere (Figure 12j-k
559 relative to 12g-h).

560 **Budget.** Time series plots of the major fluxes of the methane cycle on
561 the continental margin are shown in Figure 13. The methanogenesis rates
562 in the model output are in units of moles per meter of coastline, since it is
563 a 2-D model. We scale this up to the Siberian continental margin by
564 assuming a width of 1,000 km. The area of the shelf is then $5 \cdot 10^{11} \text{ m}^2$,
565 roughly comparable to the real shelf area of 460,000 km² [Stein and Fahl,
566 2000]. The biological rate of methane production on the continental shelf
567 evolves through time in Figure 13b. Yedoma deposition (case SL+LD)
568 tends to slowly increase the total shelf respiration rate in the model,
569 relative to a case with no land deposition (case SL). The formation of
570 permafrost, during glacial periods of case GL+LD, attenuates
571 methaneogenesis by inhibiting biological activity in the frozen soil.

572 The solid regions in Figure 13 c-h are cumulative methane sinks for six
573 different model scenarios, plotted underneath red lines showing biogenic
574 methane production. In time average, where sinks balance sources, the
575 colored areas should fill up the region below the red line.

576 Trapping of methane by impermeable permafrost leads to a spike of
577 methane fluxes at the ends of deglaciations in simulations with
578 permafrost (Figure 13 c and e). The spikes happen as sea level
579 approaches its highest extent, stifling the offshore groundwater flow by
580 decreasing the pressure head, but early in the interglacial time while
581 permafrost is the most intact. The spikes are stronger for the first glacial
582 cycles than the last, apparently due to long-term adjustment of the
583 methane cycle on the shelf (a growing together of the production rate
584 (red lines in Figure 13 c-f) and the various methane sinks (colored areas).

585 Permafrost formation blocks methane emission during times of low sea
586 level. This can be seen in the collapse of the blue regions in Figure 13 c
587 vs. d and e vs. f during times of low sea level. Blocking horizontal flow
588 disrupts offshore flow, the only significant methane sink on the shelf
589 during glacial periods (Figure 13h), resulting in somewhat higher deglacial
590 spikes of methane emission than predicted by the models including
591 transport. There is no direct link between ice fraction and methane

592 oxidation in the model, which is driven only by coexisting concentrations
593 of sulfate and methane, but the rate of methane oxidation also drops to
594 negligible during glacial times in the simulations with permafrost (grey in
595 [Figure 13 c and e](#)). The absolute rates of methane loss differ between
596 the Prefreshened vs. Marine initial conditions, but this is in part due to
597 differences in the width of the continental shelf between the two
598 simulations. The patterns of the methane cycle are very similar, however,
599 between the two cases, and also not much affected by the imposition of
600 permeable vertical channels ([Figure 13g](#)).

601 **Atmospheric Flux.** Fluxes of methane to the atmosphere are shown in
602 [Figure 14](#). In the absence of permafrost ([Figure 14 a and b](#)), or assuming
603 that bubble migration is blocked only if the ice fraction exceeds 90%, a
604 condition rarely attained in the model ([Figure 14e](#)), the highest methane
605 fluxes to the atmosphere are found during glacial (cold) times, rather
606 than warm interglacials. This is due to dissolution of methane gas into
607 the ocean when the sediment column is submerged. When permafrost
608 blocks methane gas fluxes in the sediment column, the highest
609 atmospheric fluxes are generally found during the time of early sea level
610 fall, when unfrozen sediment is exposed to the atmosphere before it has
611 a chance to freeze. The timing of the variations in atmospheric flux
612 through the glacial cycles is very sensitive to the critical ice fraction for
613 blocking gas transport ([Figure 14e](#)).

614 The impacts of the pore water salt inventory are most apparent during
615 the time of sea level fall, with permafrost formation (red lines). The
616 saltier sediment column takes about 20 kyr to choke off the methane flux
617 to the atmosphere ([Figure 14a](#)), while the pre-freshened sediment
618 column stops the methane flux more abruptly, in just a few thousand
619 years ([Figure 14b](#)). Atmospheric emissions also scale with methane
620 production rates, generally maintaining the temporal patterns of emission
621 as set by permafrost and submergence in the ocean.

622 **3.2 Anthropogenic Global Warming**

623 The atmospheric methane fluxes, shown in [Figure 15](#), increase in the
624 global warming (GW) model run, as they also do in the control (Ctl)
625 simulation, which is essentially an extended but unwarmed interglacial
626 period. The permafrost melts on a time scale of about 10,000 years for
627 the GW simulation, and about 50,000 for the Ctl. The rates of methane
628 production, and flux to the atmosphere, both increase with the loss of the

629 permafrost, if there is no change in sea level. However, the new methane
630 flux comes not as a sudden burst, but rather as a slow transition toward a
631 new, higher, chronic release rate.

632 When sea level is also changed (GW+SL), bubbles dissolve in the water
633 column, which more than counteracts the increase in methane flux due to
634 the extended interglacial (CtI) or warming (GW) scenarios.

635 **3.3 Sensitivity Studies**

636 **3.3.1 Sediment Salt Content**

637 Ice freezes until the salinity of the residual brine brings about a freezing
638 point depression equal to the in situ temperature. A saltier initial
639 sediment column will reach this condition with a lower ice fraction, its
640 melting is accelerated, and its hydrate inventory is lower (Figure 14).

641 The equilibrium salinity in the permafrost zone is not affected by the salt
642 inventory of the column, only the relative volumes of the solid and fluid
643 phases.

644 **3.3.2 Methane Production Rates**

645 The atmospheric flux increases along with either shallow, biological
646 methane production, driven by deposition of Yedoma, or thermal methane
647 production in the deep sediment column (Figure 15). Biogenic methane
648 production is too shallow in the sediment column to impact the inventory
649 of methane hydrate (Figure 11). The timing through the glacial cycles of
650 atmospheric methane emissions from these scenarios parallel each other,
651 because they are controlled in common by the transport-blocking effects
652 of permafrost and sediment submergence in the ocean.

653 **3.3.3 Geothermal Temperature Gradient**

654 When the heat flux is higher, the temperature gradient is steeper,
655 pivoting about the sediment surface temperature, which is set by the
656 ocean. The base of the methane hydrate stability boundary gets
657 shallower, while the top remains at about the same depth, resulting in a
658 thinning of the stability zone (Figure 8). The hydrate inventory through
659 the glacial cycles however is not much affected, unless the heat flux gets
660 small enough for hydrate to persist through the glaciations (Figure 11).

661

3.3.4 Thermodynamic Competition Between Ice and Hydrate

662 When ice is included as a competing phase, it excludes methane hydrate
663 from the low-pressure, very cold permafrost zone. The hydrate stability
664 zone thins (from above and below in the model: [Figure 8](#)), and the
665 hydrate inventory decreases ([Figure 11](#)). When ice formation is
666 disallowed, the hydrate stability zone approaches the sediment surface
667 during coldest glacial time, but by the time of an interglacial-based global
668 warming climate perturbation, the stability zone boundary has retreated
669 to several hundred meters below the sea floor, precluding a sudden
670 hydrate dissolution response to a suddenly warming ocean.

671

3.3.5 Permafrost Inhibition of Gas Migration

672 When the ice fraction of the model exceeds a critical threshold, gas
673 migration is blocked. Changing the value of this threshold has a strong
674 impact on the rates of methane emission during glacial versus interglacial
675 times. This process is therefore a high priority for future model
676 refinement.

677

3.3.6 Vertical flow heterogeneity

678 The chemistry of continental margin sediments in this model [*Archer et*
679 *al.*, 2012] showed a strong sensitivity to flow heterogeneity, achieved by
680 increasing the vertical permeability of every fifth grid cell. In the
681 configuration presented here, the impact of the channels is much smaller.
682 The dynamics of this simulation are thermally driven, rather than by
683 sediment deposition driving fluid flow in the continental margin case.
684 Atmospheric methane fluxes are spikier when the channels are included,
685 but the mean rate is not much changed.

686

3.3.7 Ground water Flow

687 Groundwater flow carries enough methane to be a significant sink during
688 times of low sea level. However, disabling that flow has only subtle
689 impacts on the other aspects of the methane cycle on the shelf. Spikes
690 of methane emission during late deglaciation get somewhat more intense.

691

3.4 Comparison with Observations

692 The model bubble flux to the atmosphere in the base case in analog
693 present-day conditions is 0.02 Tg CH₄ per year, which is an order of
694 magnitude lower than an estimate of the total methane emission rate

695 from the sea surface (bubbles + gas exchange) [Kort *et al.*, 2012] of 0.3
696 Tg CH₄ / yr. The model does not include gas exchange evasion of
697 methane from the sea surface, which could be significant. Concentrations
698 of methane in the water column of 50 nM are common [Shakhova *et al.*,
699 2010a], which, if they were unimpeded by sea ice, could lead to a flux
700 from the region of 0.4 Tg CH₄ / yr (assuming a typical gas exchange
701 piston velocity of 3 m/day). Gas exchange is impeded by sea ice, but it
702 can be enhanced by storms [Shakhova *et al.*, 2013]. Once released to
703 the water column, the fate of a methane molecule will depend on its
704 lifetime with respect to oxidation, which could be up to a year in the open
705 water column [Valentine *et al.*, 2001], versus its lifetime with respect to
706 gas exchange, which for ice-unimpeded conditions would be just a few
707 months for a 50-meter deep water column. Thus the methane in bubbles
708 dissolving in the water column has some chance of making it to the
709 atmosphere anyway, depending on stratification in the water column and
710 the extent of ice, and the gas exchange flux has the potential to be
711 significant in the regional total flux.

712 Methane fluxes into the water column range up to 0.4 Tg CH₄ / yr during
713 times of relatively high sea level. This is much lower than the Shakhova
714 *et al.* [2013] estimate of 17 Tg CH₄ / yr from hot-spot ebullition fluxes
715 to the water column. The model fluxes are comparable to these
716 observations when the thermal methane flux is increased by a factor of
717 100 (see [Section 3.3.2](#)), but the model lacks the physical or mechanistic
718 detail required to focus the emissions into hot spots of concentrated
719 methane flux as observed ([Section 4.1](#)).

720 **4. Discussion**

721 ***4.1 Limitations of the Model Results and Critical Issues for Future*** 722 ***Development***

723 This is the first simulation of the full methane cycle on the Siberian
724 continental margin, or any other location with embedded permafrost soils,
725 including hydrate formation and transient fluxes. It is internally
726 consistent, linking processes from the ocean, the sea floor, and the deep
727 Earth, within constraints of sediment accommodation and conservation of
728 carbon, through geologic time. As such it has some lessons to teach
729 about the real Siberian continental margin. However, many of the model
730 variables are not well known, such as the methanogenesis rates or soil
731 permeabilities, meaning that in some aspects the model results are not a

732 strong constraint on reality. These uncertainties illuminate critical issues
733 for future model refinement.

734 **4.1.1 Methane Production Rates**

735 The rates of biological and thermal methane production on the Siberian
736 continental shelf are not well constrained by laboratory measurements or
737 field inferences. These rates are treated as tunable model parameters,
738 and the sensitivity studies show that they are important ones to
739 ultimately get right.

740 **4.1.2 Gas Transport in the Sediment Column**

741 Simulating the hot-spot behavior of bubble emission from the sea floor
742 will also require more detailed treatment of the mechanisms by which gas
743 moves around in the sediment column. The model lacks faults and
744 permeable layers that act as transport highways and hydrate
745 depocenters, and may concentrate the flow into a hot-spot ebullition
746 region. The model also lacks the ability to episodically “blow out”,
747 producing the sedimentary wipe-out zones observed seismically in the
748 subsurface [*Riedel et al.*, 2002], and the pockmarks at the sediment
749 surface [*Hill et al.*, 2004]. The steady-state hydrate inventory in the
750 model is extremely sensitive to the bubble vertical transport spatial scale
751 [*Archer et al.*, 2012], which determines how far a bubble can get through
752 unsaturated conditions before it redissolves. This result demonstrates
753 the importance of gas transport to predicting the methane hydrate or
754 bubble inventories.

755 **4.1.3 Atmospheric Flux Efficiency**

756 On land, the model lacks seasonal melting of surface permafrost, and the
757 thaw bulbs underneath lakes and rivers. In the ocean, the fraction of the
758 sea-floor gas flux which dissolves in the water column intensity of water
759 column dissolution of rising bubbles depends on the bubble sizes, which
760 depend on the gas emission rate, ultimately driven by details of gas
761 transport in the sediment.

762 **4.1.4 Uncertainty in Model Output**

763 These uncertainties affect the flux of methane to the atmosphere, and
764 model predictions of the standing stocks of methane as gas and hydrate
765 in the sediment column.

766 **4.2 Robust Features of the Simulation**

767 **4.2.1 Arctic Ocean Methane Fluxes are Small in the Global Budget**

768 The model is consistent with observations [*Kort et al.*, 2012], that the
769 total atmospheric methane flux from the Siberian margin is a small
770 fraction of the global flux of methane to the atmosphere, and thus
771 represents only a minor climate forcing. The model would have to be
772 pushed very hard (as would the measurements) to fundamentally change
773 this conclusion.

774 **4.2.1 The Hydrological Salinity Ratchet**

775 Groundwater flow, driven by the pressure head, provides an advective
776 means of pumping fresh water into the subsurface sediment column that
777 has no counterpart for salty ocean water. The model lacks the mechanism
778 of salt fingering, which can enhance the diffusion of salt from above into
779 a fresh water aquifer [*Kooi et al.*, 2000]. However, higher-resolution
780 models of smaller domains that accounted for salt fingering also show a
781 time asymmetry, with faster fresh water invasion on sea level drop than
782 salt invasion on sea level rise [*Lu and Werner*, 2013; *Watson et al.*,
783 2010]. As the size of the domain increases with increasing sea level
784 change, advective processes such as hydrological flow should become
785 even more dominant over diffusive processes such as salt fingering. The
786 recent discovery of vast freshwater aquifers on global continental shelves
787 [*Post et al.*, 2013], persisting since the time of lowered sea level 20,000
788 years ago, and the lower-than-marine salinities of the pore waters
789 measured in submerged surface Arctic sediments (summarized by
790 [*Nicolisky et al.*, 2012]) are also consistent with the existence of a fresh-
791 water hydrological pump which has a significant impact on sediment
792 column salinities.

793 **4.2.2 Salinity (Water Activity) and Hydrate Stability in the Permafrost Zone**

794 In the simulations the porewater salinities in the permafrost zone did not
795 depend on the total salt content of the sediment column, but only on the
796 temperature (and secondarily pressure) condition. A saltier sediment
797 column will end up with a larger volume of brine in equilibrium than a
798 fresher sediment column would have, but the salinities of the brines would
799 be the same.

800 In the permafrost zone (low temperature and pressure), ice can tolerate
801 higher salinity (lower water activity) than methane hydrate can. As long
802 as there is no kinetic impediment to ice formation, bubbles of methane
803 rising into this zone should encounter brine salinities too high to permit
804 formation of methane hydrate.

805 **4.2.3 Sea Level Dominates the Glacial Cycle of Methane Flux**

806 The methane flux to the atmosphere through the glacial / interglacial
807 cycles is highest during cold times, because sea level is low, rather than
808 providing a positive climate feedback by releasing methane during warm
809 (high sea level) intervals. Atmospheric methane concentrations were
810 lower during glacial times than interglacials, but since the Arctic Ocean is
811 a small fraction of the total methane budget (Section 4.2.1), the
812 atmospheric concentration does not necessarily reflect Arctic fluxes.

813 **4.2.3 Methane Emission Response to Anthropogenic Climate Change**

814 There is a warming positive feedback in the simulated future from climate
815 warming, with fluxes rising gradually on a time scale of thousands of
816 years. Shakhova et al [2010b] proposed that 50 Gton C as methane
817 could erupt from the Arctic on a time scale of a few years. However, the
818 thermodynamic exclusion of methane hydrate from the permafrost zone
819 (Section 4.2.2) ensures that methane hydrate will be isolated from
820 changes in ocean temperature by ~400 meters of mud and ice. A
821 warming perturbation at the sea floor today will not reach this depth for
822 hundreds or thousands of years. A complex model is not really required
823 to conclude that methane hydrate will probably not produce a methane
824 eruption of this scale so quickly.

825 Could an abrupt methane release arise from release of trapped bubbles
826 from melting ice? The model actually does produce a glacial cycle in
827 bubble inventory, with changes exceeding 50 Gton over a cycle,
828 apparently driven by methane exclusion from ice formation (Figure 11).
829 But the model does not deliver an abrupt release in response to
830 anthropogenic warming for any of its sensitivity studies (Figure 14). We
831 would get a faster initial response to global warming if the transition from
832 glacial to global warming sediment surface temperatures hadn't mostly
833 happened thousands of years ago.

834 The model provides poor constraint on the standing stock of bubbles or
835 methane hydrate in the sediment column, and neglects many of the

836 mechanisms that could come into play in transporting methane quickly to
837 the atmosphere, such as faults, channels, and blowouts of the sediment
838 column. A continuum model such as this one predicts a smooth methane
839 release response to a warming, growing in on some e-folding time-scale.
840 A world dominated by features that each represent a small fraction of the
841 total methane reservoir will release methane more episodically, but the
842 statistical distribution of the response in time should still show the e-
843 folding time scale of the underlying driving mechanism, the diffusion of
844 heat into the sediment column.

845 The way to deliver 50 Gton of methane to the atmosphere on a short
846 time scale is for it all to be released from a single geologic feature pent
847 up by ice. But 50 Gton of C represents a large fraction of all the
848 traditional natural gas deposits on Earth (about 100 Gton C). The place
849 to look for such a large unstable gas reservoir is in the field, not in this
850 model, but until such a thing is found it remains conjecture.

851 On time scales of thousands of years and longer, carbon from deep
852 methane hydrates and frozen organics on the Siberian continental shelf
853 could reach the atmosphere / ocean carbon cycle, potentially significantly
854 amplifying the “long tail” climate impact of anthropogenic carbon release.
855 Methane that is oxidized in the ocean would eventually equilibrate with
856 the atmosphere, so it is much easier for escaping methane to impact the
857 long tail as CO₂ than it is to affect the near future as methane.

858 The potential for future sea level change is much higher on millennial time
859 scales than the forecast for the year 2100, because it takes longer than
860 a century for ice sheets to respond to changes in climate. The model
861 finds that for the future, if sea level changes by tens of meters, as guided
862 by paleoclimate reconstructions [*Archer and Brovkin, 2008*], the impact
863 of sea level rise could overwhelm the impact of warming. The dominance
864 of sea level over temperature in the model of this area is due to
865 dissolution of methane in the water column, rather than a pressure effect
866 on hydrate stability, which is generally a weaker driver than ocean
867 temperature in deeper-water settings [*Mienert et al., 2005*].

868 **5. Acknowledgements**

869 This paper benefited from constructive reviews by Dmitri Nicolsky and
870 two anonymous reviewers, contributed comments by Natalia Shakhova,
871 Igor Semiletov, and Vladimir Tumskey, and the efforts of the editor

872 Laurent Bopp.

873 **6. Bibliography**

874 Archer, D., and V. Brovkin, The millennial lifetime of fossil fuel CO₂,
875 *Climatic Change*, 90, 283-297, 2008.

876 Archer, D.E., B.A. Buffett, and P.C. McGuire, A two-dimensional model of
877 the passive coastal margin deep sedimentary carbon and methane
878 cycles, *Biogeosciences*, 9, 1-20, 2012.

879 Archer, D.E., M. Eby, V. Brovkin, A.J. Ridgwell, L. Cao, U. Mikolajewicz, K.
880 Caldeira, H. Matsueda, G. Munhoven, A. Montenegro, and K. Tokos,
881 Atmospheric lifetime of fossil fuel carbon dioxide, *Ann. Reviews*
882 *Earth Planet Sci.*, 37, 117-34, 2009.

883 Hill, J.C., N.W. Driscoll, J.K. Weissel, and J.A. Goff, Large-scale elongated
884 gas blowouts along the US Atlantic margin, *Journal of Geophysical*
885 *Research-Solid Earth*, 109 (B9), 2004.

886 Kooi, H., J. Groen, and A. Leijnse, Modes of seawater intrusion during
887 transgressions, *Water Resources Res.*, 36 (12), 3581-3589, 2000.

888 Kort, E.A., S.C. Wofsy, B.C. Daube, M. Diao, J.W. Elkins, R.S. Gao, E.J.
889 Hintsa, D.F. Hurst, R. Jimenez, F.L. Moore, J.R. Spackman, and M.A.
890 Zondlo, Atmospheric observations of Arctic Ocean methane
891 emissions up to 82 degrees north, *Nature Geoscience*, 5 (5), 318-
892 321, 2012.

893 Lu, C., and A.D. Werner, Timescales of seawater intrusion and retreat,
894 *Advances in Water Resources*, 59, 39-51, 2013.

895 Martin, P.A., D.W. Lea, Y. Rosenthal, N.J. Shackleton, M. Sarnthein, and T.
896 Papenfuss, Quaternary deep sea temperature histories derived from
897 benthic foraminiferal Mg/Ca, *Earth and Planetary Science Letters*,
898 198 (1-2), 193-209, 2002.

899 Mienert, J., M. Vanneste, S. Bunz, K. Andreassen, H. Hafliðason, and H.P.
900 Sejrup, Ocean warming and gas hydrate stability on the mid-
901 Norwegian margin at the Storegga Slide, *Marine and Petroleum*
902 *Geology*, 22 (1-2), 233-244, 2005.

- 903 Nicolsky, D.J., V.E. Romanovsky, N.N. Romanovskii, A.L. Kholodov, N.E.
904 Shakhova, and I.P. Semiletov, Modeling sub-sea permafrost in the
905 East Siberian Arctic Shelf: The Laptev Sea region, *Journal of*
906 *Geophysical Research-Earth Surface*, 117, 2012.
- 907 Post, V.E.A., J. Groen, H. Kooi, M. Person, S.M. Ge, and W.M. Edmunds,
908 Offshore fresh groundwater reserves as a global phenomenon,
909 *Nature*, 504 (7478), 71-78, 2013.
- 910 Riedel, M., G.D. Spence, N.R. Chapman, and R.D. Hyndman, Seismic
911 investigations of a vent field associated with gas hydrates, offshore
912 Vancouver Island, *Journal of Geophysical Research-Solid Earth*, 107
913 (B9), 2002.
- 914 Shakhova, N., I. Semiletov, I. Leifer, V. Sergienko, A. Salyuk, D. Kosmach,
915 D. Chernykn, C. Stubb, D. Nicolsky, V.E. Tumskey, and O.
916 Gustafsson, Ebullition and storm-induced methane release from the
917 East Siberian Arctic shelf, *Nature Geoscience*, DOI:
918 10.1038/NGEO2007, 2013.
- 919 Shakhova, N., I. Semiletov, A. Salyuk, V. Yusupov, D. Kosmach, and O.
920 Gustafsson, Extensive Methane Venting to the Atmosphere from
921 Sediments of the East Siberian Arctic Shelf, *Science*, 327 (5970),
922 1246-1250, 2010a.
- 923 Shakhova, N.E., V.A. Alekseev, and I.P. Semiletov, Predicted methane
924 emission on the East Siberian shelf, *Doklady Earth Sciences*, 430
925 (2), 190-193, 2010b.
- 926 Stein, R., and K. Fahl, Holocene accumulation of organic carbon at the
927 Laptev Sea continental margin (Arctic Ocean): sources, pathways,
928 and sinks, *Geo-Marine Letters*, 20 (1), 27-36, 2000.
- 929 Stouffer, R.J., and S. Manabe, Equilibrium response of thermohaline
930 circulation to large changes in atmospheric CO2 concentration,
931 *Clim. Dynamics*, 20, 759-773, 2003.
- 932 Valentine, D.L., D.C. Blanton, W.S. Reeburgh, and M. Kastner, Water
933 column methane oxidation adjacent to an area of active hydrate
934 dissociation, Eel River Basin, *Geochimica Et Cosmochimica Acta*, 65
935 (16), 2633-2640, 2001.

936 Watson, T.A., A.D. Werner, and C.T. Simmons, Transience of seawater
937 intrusion in response to sea level rise, *Water Resources Res.*, 40
938 (W12533), doi:10.1029/2010WR009564, 2010.

939

940 7. Figure Captions

941 Figure 1. Domain of the model as applied to the Laptev Sea continental
942 shelf and slope. This is the result of 62 million years of sediment
943 accumulation on the crust, isostatic subsidence, pore fluid flow, and
944 thermal diffusion, used as the initial condition for glacial / interglacial
945 cycle and climate change simulations. Color indicates temperature. a)
946 Full view. Black line shows the bottom of the crust, which grades
947 smoothly from continental on the left into ocean crust through most of
948 the domain on the right. b) Zoom in to see increased model resolution in
949 the upper kilometer of the sediment column.

950 Figure 2. Pore water salinity a) The fully marine case, in which the
951 sediment column has always been submerged underneath a time-invariant
952 sea level. b) Result of sediment column freshening by hydrological
953 groundwater flow, driven by the pressure head resulting from a water
954 table higher than sea level. A movie of the transition from marine to
955 freshened (the origin of b) can be seen at
956 http://geosci.uchicago.edu/~archer/spongebob_arctic/fig2.movie.gif

957 Figure 3. Particulate Organic Carbon (POC) concentration. Highest values
958 are found in the sediment depocenter just off the continental shelf break.

959 Figure 4. Initial distribution of dissolved methane. a) Concentration in
960 moles/m³. b-d) $\Omega = \text{CH}_4 / \text{CH}_{4(\text{sat})}$ deviation from equilibrium, b) of the
961 Marine (salty) initial condition; c) of the pre-freshened initial condition
962 (note depletion in near-surface near-shore sediments in the upper left);
963 d) including permeable channels every five grid points, plus pre-
964 freshening.

965 Figure 5. Time-dependent forcing for the glacial / interglacial simulations
966 and the global warming scenarios. a) Sea level is imposed as a sawtooth
967 100-kyr cycle, with interglacial intervals shaded. The GW+S simulation
968 tracks potential changes in sea level on long time scales due to fossil fuel
969 CO₂ release, following a covariation from the geologic past of 15 meters /

970 °C. The GW and Control simulations hold sea level at interglacial levels.
971 b) Ocean temperature forcings.

972 Figure 6. Colors indicate salinity in the unfrozen pore fluid of the sediment
973 column. Thin solid black contours show the frozen fraction of the pore
974 space. Heavy black stippled contour shows the stability boundary of
975 methane hydrate as a function of temperature, pressure, and unfrozen
976 pore fluid salinity. Left side: previously pre-freshened initial condition.
977 Right side: Pure marine initial condition. c-d) Lowered sea level (from 70
978 kyr in Figure 8) but warm air temperatures prevent permafrost formation.
979 e-f) Glacial conditions of lowered sea level (70 kyr) and atmospheric
980 temperature of -17 °C driving permafrost formation. The pre-freshened
981 and the marine initial conditions differ in the frozen fraction of sediment,
982 but the salinity of the unfrozen fluid, a correlate of the activity of water,
983 depends only the temperature. g-h) Rising sea level (at 90 kyr in Figure
984 8) into an interglacial interval. Movies of the glacial cycles (GL) with the
985 prefreshened initial condition can be seen at
986 http://geosci.uchicago.edu/~archer/spongebob_arctic/fig6a.movie.gif ,
987 and the marine initial condition at
988 http://geosci.uchicago.edu/~archer/spongebob_arctic/fig6b.movie.gif.

989 Figure 7. Pore fluid pressure forcing and flow through the glacial cycles.
990 Left) Colors indicate $P_{\text{excess}} + P_{\text{head}}$, solid contours are ice fraction, dashed
991 contours are P_{head} . Right) Colors indicate $P_{\text{excess}} + P_{\text{head}}$, note different color
992 scale from Left. Initial refers to the prefreshened initial condition. “Low
993 Sea Level” refers to simulation SL. “Glacial” and “Interglacial” refer to
994 simulation GL. Dashed contours indicate ice fraction, vectors fluid
995 velocity. Movies can be seen at
996 http://geosci.uchicago.edu/~archer/spongebob_arctic/fig7a.movie.gif
997 and
998 http://geosci.uchicago.edu/~archer/spongebob_arctic/fig7b.movie.gif.

999 Figure 8. Sensitivities of the hydrate stability zone. Impact of the
1000 competition between ice and hydrate phases (a-d), and the geothermal
1001 temperature gradient (e-f). When ice is included as a potential solid
1002 phase, the pore waters are salty in the permafrost zone (a), restricting
1003 hydrate stability to at least 300 meters below sea level throughout the
1004 simulation (c). When ice is forbidden to form, hydrate can be stable
1005 nearly to the sediment surface during the height of the glaciation (b and
1006 d). The base of the stability zone is sensitive to the geothermal
1007 temperature gradient, while the shallowest reach of the stability zone

1008 does not respond to changing heat fluxes, because the temperatures are
1009 “anchored” at the ocean value at the top of the sediment column.

1010 Figure 9. Dissolved methane concentration relative to equilibrium ($\Omega =$
1011 $\text{CH}_4 / \text{CH}_{4(\text{sat})}$). Solid contours indicate ice fraction, dashed contours show
1012 the methane hydrate stability boundary. Movies for the left, center, and
1013 right columns, respectively can be seen at
1014 http://geosci.uchicago.edu/~archer/spongebob_arctic/fig9a.movie.gif ,
1015 http://geosci.uchicago.edu/~archer/spongebob_arctic/fig9b.movie.gif ,
1016 and
1017 http://geosci.uchicago.edu/~archer/spongebob_arctic/fig9c.movie.gif.

1018 Figure 10. Carbon cycle through glacial cycles from a prefreshened initial
1019 condition. Solid contours: Ice Fraction. Dashed contours: Methane
1020 hydrate stability zone. Left) Particulate organic carbon (POC)
1021 concentration. Movie at
1022 http://geosci.uchicago.edu/~archer/spongebob_arctic/fig10a.movie.gif.
1023 Center) Biological methane production rate. Movie at
1024 http://geosci.uchicago.edu/~archer/spongebob_arctic/fig10b.movie.gif
1025 Right) Methane hydrate concentration. Movie at
1026 http://geosci.uchicago.edu/~archer/spongebob_arctic/fig10c.movie.gif.
1027 Movies of methane hydrate stability and concentration are given for the
1028 sensitivity studies, in the supplemental material and at
1029 <http://geosci.uchicago.edu/~archer/spongebob/>.

1030 Figure 11. Glacial cycle of methane hydrate inventory on the continental
1031 shelf. a) Effects of salt and ice. b) Sensitivity to methaneogenesis rates.
1032 c) Sensitivity to the column temperature gradient. d) Glacial cycles of
1033 shelf bubble inventories, effects of salt and ice.

1034 Figure 12. Spatial distribution and sea level impact of methane fluxes to
1035 the atmosphere. a-d) Solid line shows the elevation of the sediment
1036 surface relative to the sea level at the time. Grey lines (scale to right)
1037 show the efficiency of bubble transport through the water column,
1038 assuming a flux attenuation length scale of 30 meters. e-k) Dashed line:
1039 Methane bubble flux across the sediment surface. Solid line: Methane
1040 bubble flux to the atmosphere (dashed line multiplied by transport
1041 efficiency). Most of the methane flux in the model occurs near the shelf
1042 break, and submergence in the ocean has a strong impact on the flux to
1043 the atmosphere. A related movie can be seen at
1044 http://geosci.uchicago.edu/~archer/spongebob_arctic/fig12.movie.gif .

1045 Figure 13. Glacial / interglacial cycle of methane fluxes on the
 1046 continental margin of the model. Sea level at top, grey regions indicate
 1047 interglacial intervals, pink the Anthropocene. a-e) Cumulative methane
 1048 fluxes. Red lines show production rate. Brown regions show lateral
 1049 transport of dissolved methane. Grey shows oxidation by SO_4^{2-} in the
 1050 sediment column. Blue shows bubble flux to the water column. During
 1051 interglacial times (e.g. far left) there is a small onshore transport of
 1052 methane, which is represented by a negative starting point for the
 1053 oxidation (grey) region. In equilibrium, the colored areas should fill in the
 1054 region under the red curve.

1055 Figure 14. Methane fluxes to the atmosphere. Sea level at the top,
 1056 interglacial intervals in vertical grey bars, the Anthropocene in pink. a)
 1057 From a pre-freshened initial condition, with and without permafrost
 1058 formation. b) From a pure marine initial condition. c and d) Sensitivity to
 1059 terrestrial organic carbon deposition during low sea-level stands, and to
 1060 thermogenic methane flux. e) Sensitivity to the impact of ice fraction on
 1061 bubble mobility.

1062 Figure 15. Impact of anthropogenic warming on the methane cycle in the
 1063 model. a) Base cases, a warming scenario (GW), without and with a
 1064 geological time-scale sea level rise scenario (+SLR), and extended
 1065 interglacial control (Ctl). Warming plus increasing sea level decreases the
 1066 methane flux overall, due to bubble dissolution in a deeper water column.
 1067 b) Altered model physics impacts. c and d) Altered methanogenesis
 1068 rates. e) Sensitivity to the ice fraction at which bubble mobility is
 1069 assumed stopped.

1070 8. Tables

1071 Table 1. Nomenclature describing the model scenarios and sensitivity
 1072 runs.

Fr	The sediment column has been pre-freshened by previous exposure to hydrological forcing.
Mr	Initial salinities are close to marine.
SL	Sea level changes with constant air and water temperatures
GL	SL + glacial cycles in air and water

	temperature
GW	A long-term global warming scenario, a peak and long tail temperature perturbation consistent with CO ₂ release and cessation of the glacial sawtooth forcing.
GW+SL	Adds geologic-timescale sea level rise due to anthropogenic climate change, based on correlation between temperature and sea level in the geologic past (10 meters / °C).
Ctl	An extended interglacial with no CO ₂ release forcing.
+ LD	Land deposition of carbon-rich Yedoma. Base case is 10 m / 100 kyr, with sensitivity runs using 30 and 100 m / 100 kyr accumulation of 30% POC material. Movies in the supplemental material are identified by the tags Land30 and Land100.
+ TG	Thermogenic methane production rate sensitivity runs, scaling the rate from the spinup result by factors of 10 and 100. Movies in the supplemental material are identified by the tags TGenX10 and TGenX100.
+ Geotherm	Sensitivity of ice and hydrate cycles on the geothermal temperature gradient. Temperatures from the Base simulation were adjusted when calculating the stability of ice and hydrate, to simulate the impact of geothermal heat fluxes on hydrate stability. Note that other aspects of the sediment column, including the solubility of methane, retained the original temperatures. Heat fluxes simulated include 25 mW/m ² , 37.5, 50 (Base), 62.5, and 75. Movies of the non-base runs are identified by tags HF050,

	HF075, HF125, and HF150.
Ice and Bubble Transport	When the ice fraction exceeds a threshold value methane gas flow is disabled. Base case is 50%, variants 10%, 30%, 70%, and 90%, identified with tags Ice10, Ice30, Ice70, and Ice90.
No Ice	The ice phase is disallowed in the thermodynamic calculation. Movies in the supplemental material include salinity. The files are tagged as NoIce
No Salt from Ice	Ice is allowed to form, but it does not affect the salinity as it determines methane hydrate stability. Movie files are tagged as NoSalFromIce.
Permeable Channels	Increasing vertical permeability by a factor of 10 every 5 th grid cell, to generate heterogeneity in the flow. Tagged as PermChan
No Horizontal Flow	Horizontal flow is disabled. Tagged as NoHFlow.

1073 Movies comparing altered scenario runs with the Base scenario are given
1074 in the supplemental material, and at
1075 <http://geosci.uchicago.edu/~archer/spongebob/>. Movies named
1076 hydrate* and bubbles* show methane hydrate and bubble inventories and
1077 stability zone changes. Files entitled salinity* show salinities, and
1078 bubb_atm* show bubble fluxes through and out of the sediment column,
1079 into the ocean, and into the atmosphere, through time.

1080

1081 **9. Supplemental Text**

1082 ***S1. Vertical Flow***

1083 In previous versions of the SpongeBOB model, the fluid flow was
1084 calculated explicitly, each time step, as a function of P_{excess} at the
1085 beginning of the time step. Numerical stability motivated a modification
1086 of the vertical flow to an implicit numerical scheme, which finds by
1087 iteration an internally consistent array of vertical flow velocities and
1088 resulting P_{excess} values from a time point at the end of the time step.
1089 Ocean and atmosphere models often use this methodology for vertical
1090 flow. A benefit to this change is stability in the vertical flow field,
1091 reducing numerical noise that can cause trouble with other aspects of the
1092 model such as ice formation. Implicit schemes can be more efficient
1093 computationally, but in this case the execution time is not improved by
1094 the implicit method, just the stability.

1095 Note that the flow scheme in its formulation is entirely elastic, whereas in
1096 reality, pore fluid excluded by the pressure of a sediment column above
1097 sea level, for example, where it is uncompensated by buoyancy in
1098 seawater, should remain excluded when sea level rises again, like
1099 toothpaste from the tube. However, my attempts to embed this plastic
1100 behavior into an implicit solver failed to converge.

1101 ***S2. Ice Formation***

1102 The ice content in a grid cell relaxes toward equilibrium, quickly enough to
1103 approximate an equilibrium state through the slow temperature evolution
1104 in the model (which neglects a seasonal cycle at the surface), but slowly
1105 enough to avoid instabilities with other components of the model such as
1106 fluid flow and methane hydrate formation. A limiter in the code prevents
1107 more than 99% of the fluid in a grid cell from freezing, but the
1108 thermodynamic equilibrium salinity is used to calculate, for example, the
1109 stability of methane hydrate, to prevent the numerical limiter from
1110 affecting the thermodynamic availability of water to drive chemical
1111 reactions.

1112 ***S3. Thermodynamics of Ice and Hydrate***

1113 When the system consists only of ice and fluid phases, the equilibrium
1114 salinity S_{eq} increases with decreasing temperature below freezing (**Figure**
1115 **1a**, left). Above the melting temperature, ice is unstable, as indicated by

1116 the nonzero values of the disequilibrium temperature, $\Delta T_{\text{eq, ice}} = T - T_{\text{eq, ice}}$,
1117 in contours, even in zero-salinity water (right). For a system consisting
1118 of only the hydrate and fluid phases (assuming that ice formation is
1119 disallowed, and also gas saturation for methane) (Figure 1b), the behavior
1120 is similar but with an added pressure dependence due to the
1121 compressibility of the gas phase.

1122 When both solid phases are allowed, the overall equilibrium salinity will
1123 whichever is higher between $S_{\text{eq, ice}}$ and $S_{\text{eq hydrate}}$. Whichever phase can
1124 seize water at its lowest activity (highest salinity) will be the stable
1125 phase. The salinity of the brine excluded from that phase will be too high
1126 to permit the existence of the other solid phase at that temperature.
1127 The contours show ΔT_{eq} for hydrate (solid) and ice (dashed), which are
1128 also plotted in color in Figures 1d and e. This is illustrated in Figure 1d, in
1129 colors of $\Delta T_{\text{eq, hydrate}}$ and contours of the excess salinity relative to hydrate
1130 equilibrium, $S_{\text{max}} - S_{\text{eq, hydrate}}$. Hydrate is only stable when $\Delta T_{\text{eq, hydrate}}$ is zero
1131 (purple color).

1132 Under permafrost conditions of low pressure and low temperature (upper
1133 left corner), $\Delta T_{\text{eq, hydrate}}$ is greater than zero, indicating that hydrate is
1134 unstable, coinciding with the salinity forcing from the ice, in overlain
1135 contours. A similar exclusion of ice in part of the hydrate stability zone is
1136 seen Figure 1e, but this would only happen in nature in conditions of
1137 unlimited methane. The resulting phase diagram for ice and methane
1138 hydrate is shown in Figure 1f. Hydrate stability is suppressed in the
1139 permafrost zone by this thermodynamic mechanism.

1140 There is an analogous exclusion of ice from part of the methane hydrate
1141 stability zone, but this assumes unlimited methane; if the dissolved
1142 methane concentration is less than gas saturation, both solid phases can
1143 coexist. In the permafrost zone, the dissolved methane concentration
1144 cannot exceed solubility with gas saturation, so the exclusion of methane
1145 hydrate from thermodynamic stability is inescapable.

1146 ***S4. Construction of the Pre-Freshened Sediment Column***

1147 If sea level falls, exposing the sediment column to the atmosphere for the
1148 first time, there is a pressure head gradient extending throughout the
1149 sediment column, provoking lateral flow at all depths. As the pore fluid at
1150 the surface is replaced by fresh runoff, the lighter density of that fluid
1151 tends to diminish the pressure head gradient in the deeper sediment

1152 column. The deeper pressure gradient and flow approach zero as the
1153 fresh water lens in the outcropping region approaches an isostatic
1154 equilibrium condition known as the Ghyben-Herzberg relation [*Moore et*
1155 *al.*, 2011], in which each meter elevation of the water table is
1156 compensated for by about 40 meters of fresh water below sea level,
1157 determined by the difference in densities of fresh and salt water.

1158 To create this condition within the model, two simulations are presented
1159 in which sea level was decreased by 30 and 120 meters, respectively, and
1160 held there for millions of years (**Supplemental Figure 2**). The 30-meter
1161 drop experiment produced land outcrop in about 1/4 of the model
1162 domain, with the predicted equilibrium Ghyben-Herzberg halocline
1163 reaching about 1200 meters maximum depth. The model salinity relaxes
1164 into close agreement with the predicted halocline, lending support to the
1165 model formulation for density, pressure head, and fluid flow. As time
1166 progresses further, the outcropping land surface subsides (there is no
1167 land deposition in this scenario), until it drops below the new lowered sea
1168 level value after about 2.5 Myr. The hydrological pumping generates a
1169 low-methane plume that also persists for millions of years in the model
1170 (**Supplemental Figure 3**).

1171 **negligible impact of canyons**

1172 Variants of this experiment were done with differing values of the lateral
1173 distance to drainage canyons in the model, which provide a pathway for
1174 fluid loss in sediments above sea level. When a hypothetical canyon is
1175 located 10 km from the SpongeBOB slab, the model salinity approaches
1176 equilibrium on an e-folding time scale of about 400 kyr (**Supplemental**
1177 **Figure 4**). When the canyon is 100 km distant or nonexistent, the
1178 equilibration time scale is about 600 kyr. Based on the idea that canyons
1179 of order 100 km long should be about 100 km apart, the Base simulation
1180 in this paper assumes canyon spacing of 100 km.

1181 **120 m same as 30**

1182 When sea level is lowered by 120 m, the sequence of events is similar,
1183 except that the pressure head is so high that to satisfy the Ghyben-
1184 Herzberg relation would require fresh pore waters at many kilometers
1185 depth, even deeper than bedrock on the “continental” side of the model
1186 domain. Because of the low permeability of the deepest sediment
1187 column, the freshwater pumping groundwater mechanism is unable to

1188 reach these deepest pore waters, which therefore remain salty. The time
1189 scale for establishing a significant freshening of the upper kilometer of
1190 the sediment column is still on the order of 100-500 kyr, and the
1191 subsequent subsidence time of the sediment column in the model, until it
1192 drops below the new lowered sea level, takes about 10 Myr. In both
1193 cases, subsidence of the exposed sediment column prevents the
1194 sediment surface in the model from remaining above sea level indefinitely
1195 (without land deposition).

1196 **10. Supplemental Figure Captions**

1197 Supplemental Figure 1. Thermodynamics of hydrate and ice. Top) Colors
1198 are salinities, which range from fresh if there is no solid phase, to saltier
1199 as the freezing point depression of the solid phase follows the in situ
1200 temperature. Contours indicate the extent of thermal disequilibrium, ΔT_{eq}
1201 $= T - T_{eq}$. a) For the system of ice and fluid. b) Considering hydrate and
1202 fluid phases, excluding ice formation and assuming equilibrium with
1203 methane gas. c) Combined ice + hydrate + fluid system, where the
1204 salinity is controlled by the most stable solid phase. Solid contours are
1205 $\Delta T_{eq, hydrate}$, dashed $\Delta T_{eq, ice}$. d and e) Colors are ΔT_{eq} , where 0 (purple)
1206 indicates stability, and contours are the excess salinity relative to a solid
1207 phase, e.g. $S_{max} - S_{eq, hydrate}$ in (d), for hydrate, and e) ice. f) Phase diagram
1208 for the ice + hydrate + brine system. Hydrate is excluded from the ice
1209 phase space by the high salinity of the brine. Ice is ideally also excluded
1210 from part of the hydrate stability zone by a similar mechanism, but this
1211 would only happen in nature under conditions of unlimited methane
1212 availability. Thus it is easier to envision coexistence of hydrate and ice
1213 within the hydrate stability zone, under conditions of limited methane
1214 availability, than it is to imagine hydrate in the permafrost zone, where
1215 ice has no impediment for formation.

1216 Supplemental Figure 2. Freshening the sediment column by hydrological
1217 groundwater flushing. Color indicates salinity. Solid black line represents
1218 sea level in the ocean (white space), and the equilibrium fresh-salty
1219 boundary given a snapshot of the pressure head (the Ghyben-Herzberg
1220 relation). Left side: results of dropping sea level 30 meters and holding it
1221 there. A freshwater lens forms and strives to reach Ghyben Herzberg
1222 equilibrium as the sediment column subsides, where atmospheric
1223 exposure decreases its buoyancy and stops sediment accumulation.
1224 After the sediment column subsides beneath the still-lowered sea level,
1225 the fresh water lens remains for millions of years. A movie can be seen at

1226 http://geosci.uchicago.edu/~archer/spongebob_arctic/supp_fig2a.movie
1227 [.gif](#) . Right side: Result of dropping sea level 120 meters and holding it
1228 there forever. Movie at
1229 http://geosci.uchicago.edu/~archer/spongebob_arctic/supp_fig2b.movie
1230 [.gif](#)

1231 Supplemental Figure 3. Dissolved methane impact by hydrological
1232 freshening of the sediment column as described in **Supplemental Figure 2**.
1233 $\Omega = \text{CH}_4 / \text{CH}_{4(\text{sat})}$. Movies can be seen at
1234 http://geosci.uchicago.edu/~archer/spongebob_arctic/supp_fig3a.movie
1235 [.gif](#) and
1236 http://geosci.uchicago.edu/~archer/spongebob_arctic/supp_fig3b.movie
1237 [.gif](#)

1238 Supplemental Figure 4. Time scale of depleting the salinity of the
1239 continental shelf sediment column after an instantaneous sea level drop
1240 of 30 meters. The effect of lateral canyons is to provide a pathway for
1241 saline fluid to be replaced by fresh groundwater in sediments above sea
1242 level. If the lateral canyon spacing is 10 km, they can have a significant
1243 impact on the time constant for ground water flushing. A more
1244 conservative 100-km canyon is adopted for the rest of the simulations.

1245

1246

1247

1248

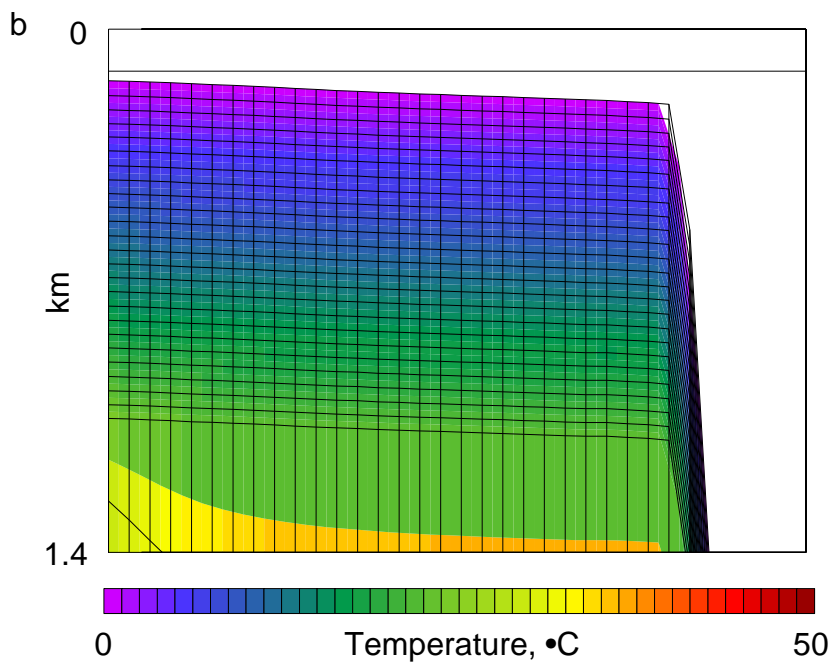
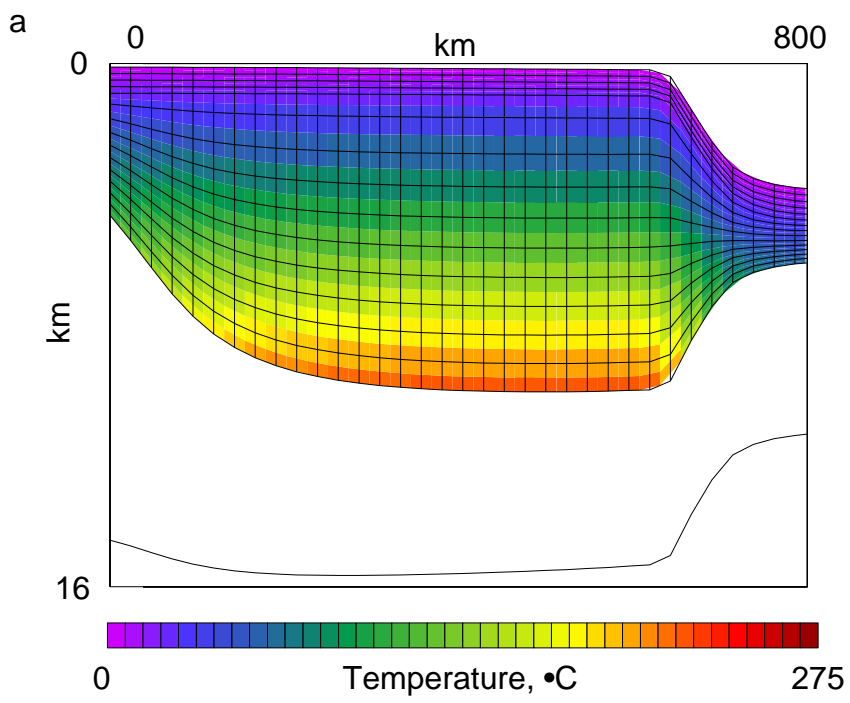


Figure 1

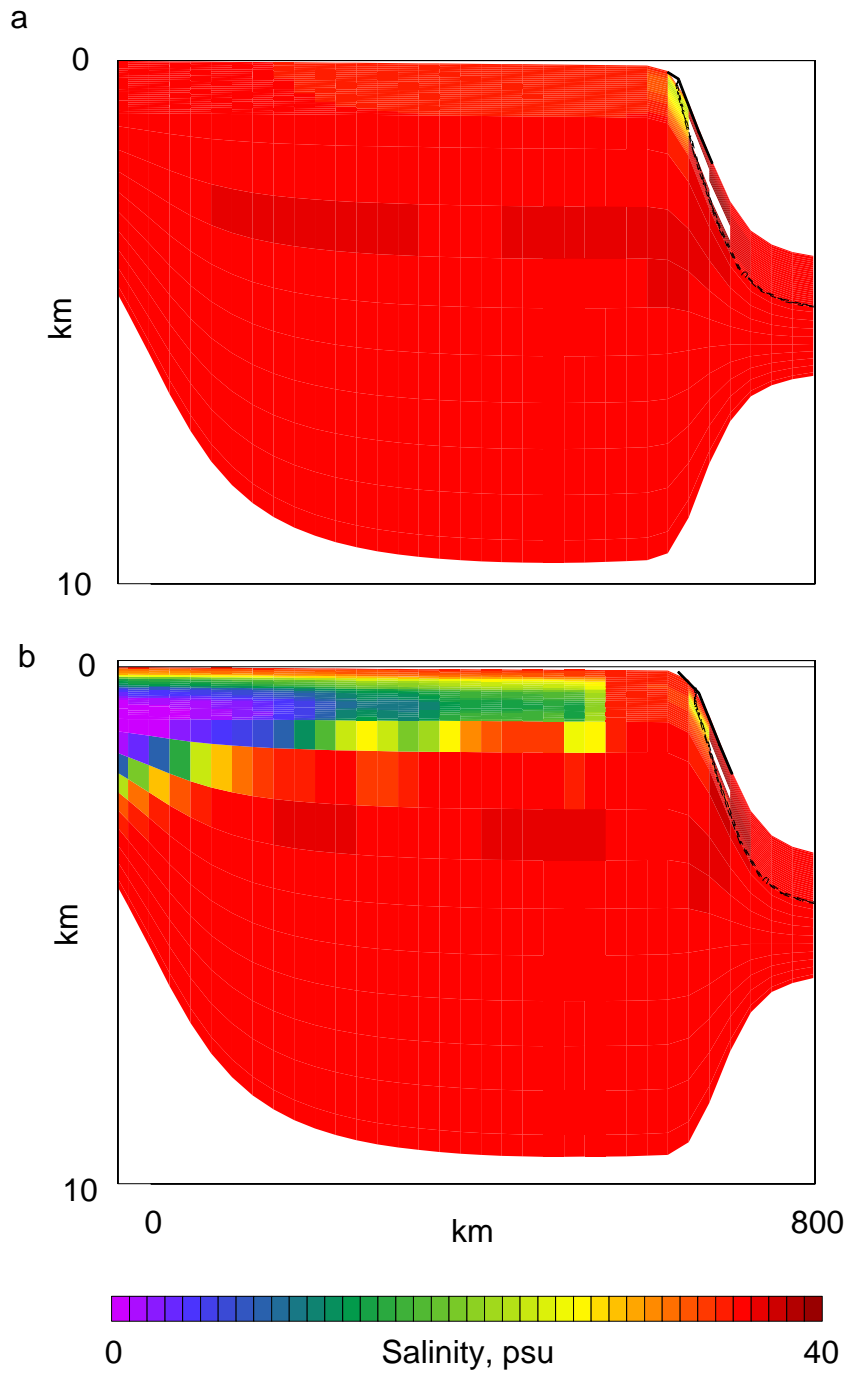


Figure 2

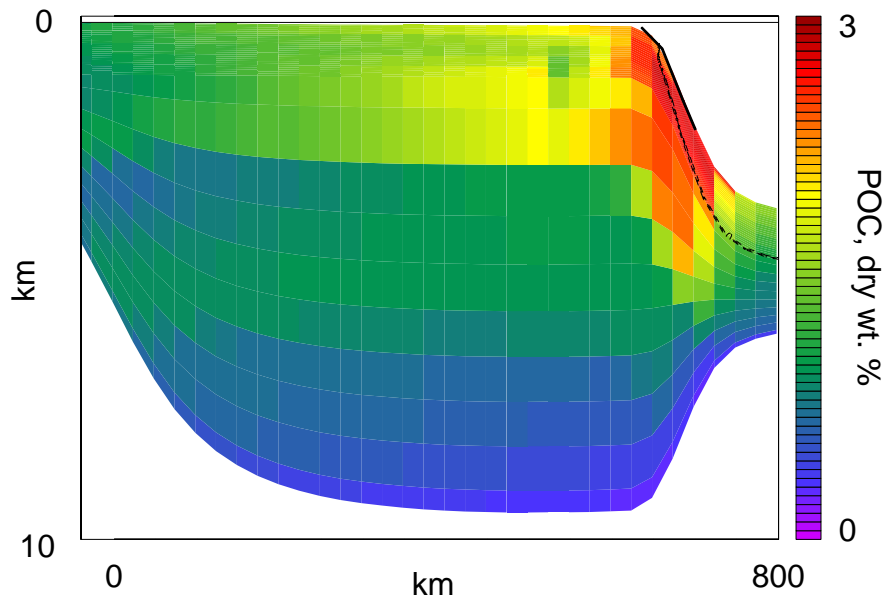


Figure 3

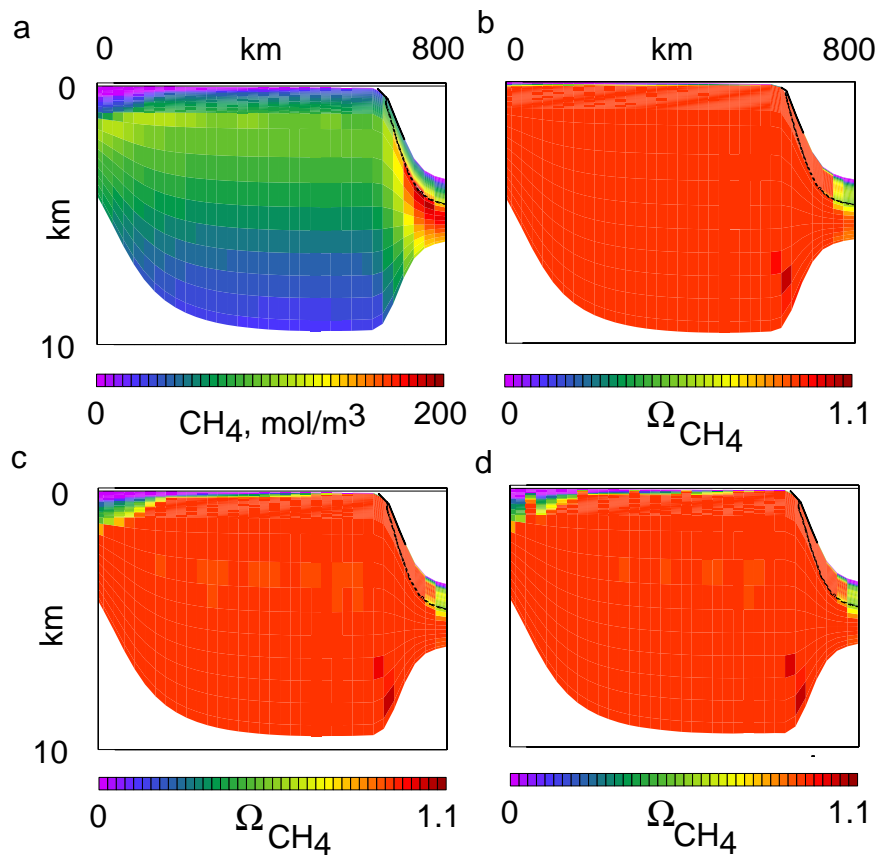


Figure 4

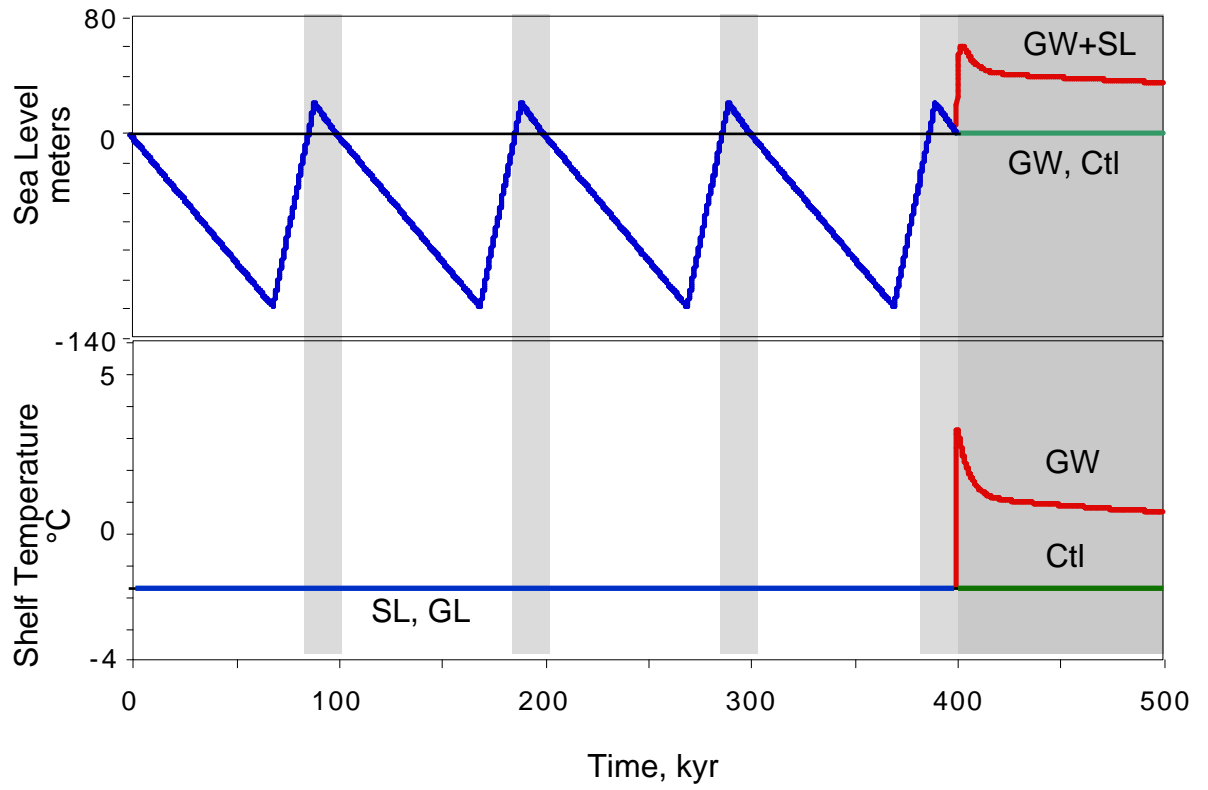


Figure 5

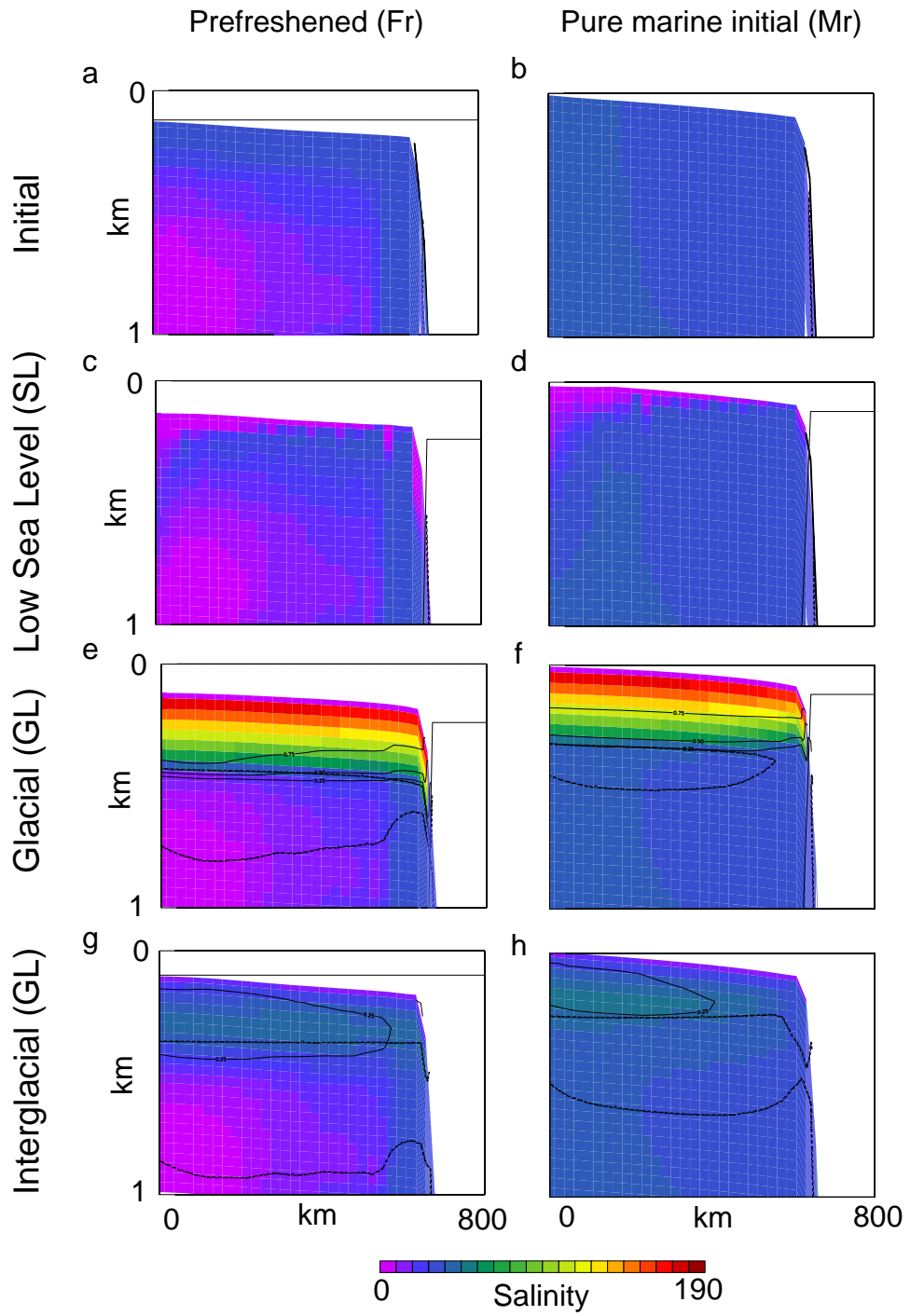


Figure 6

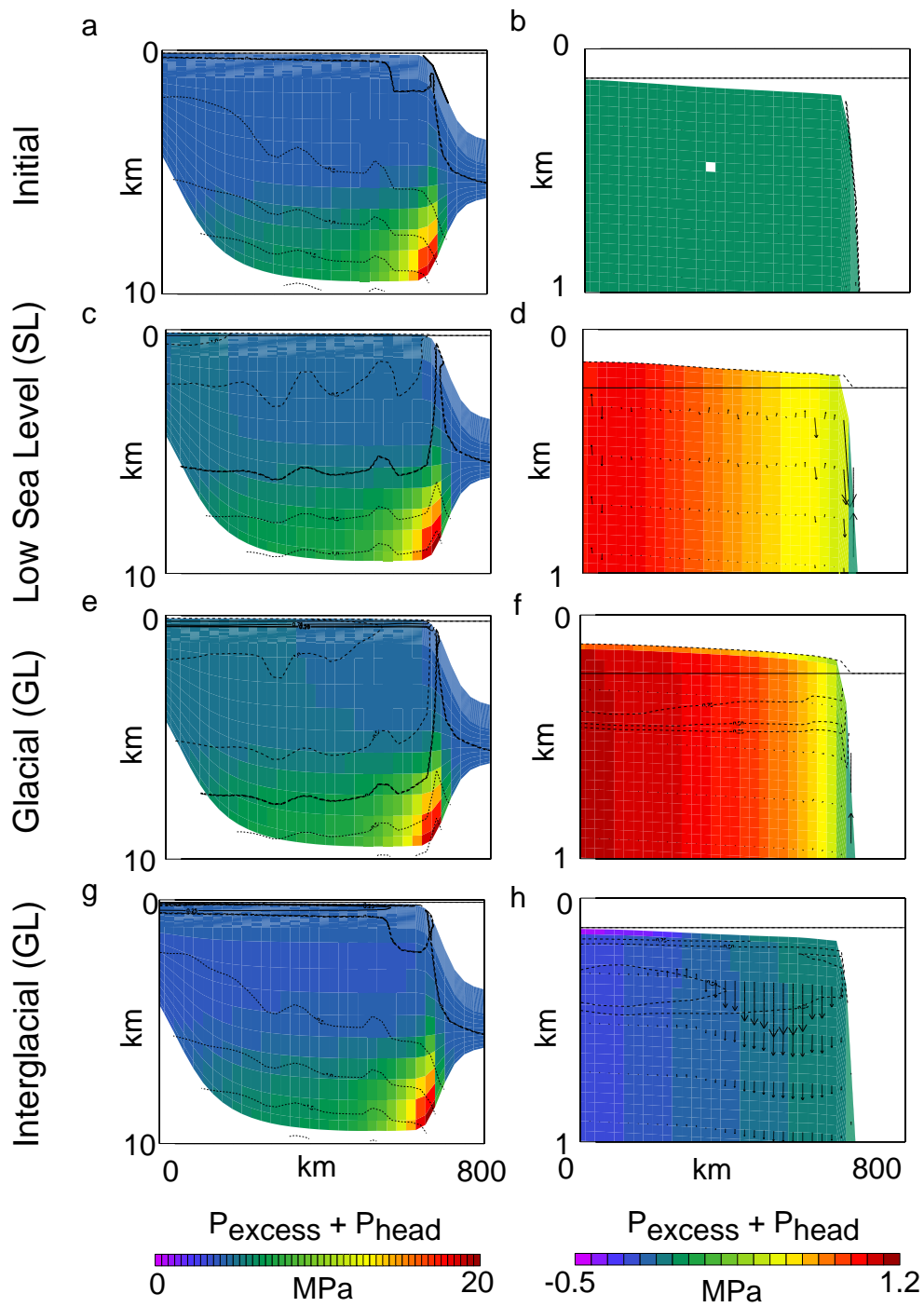


Figure 7

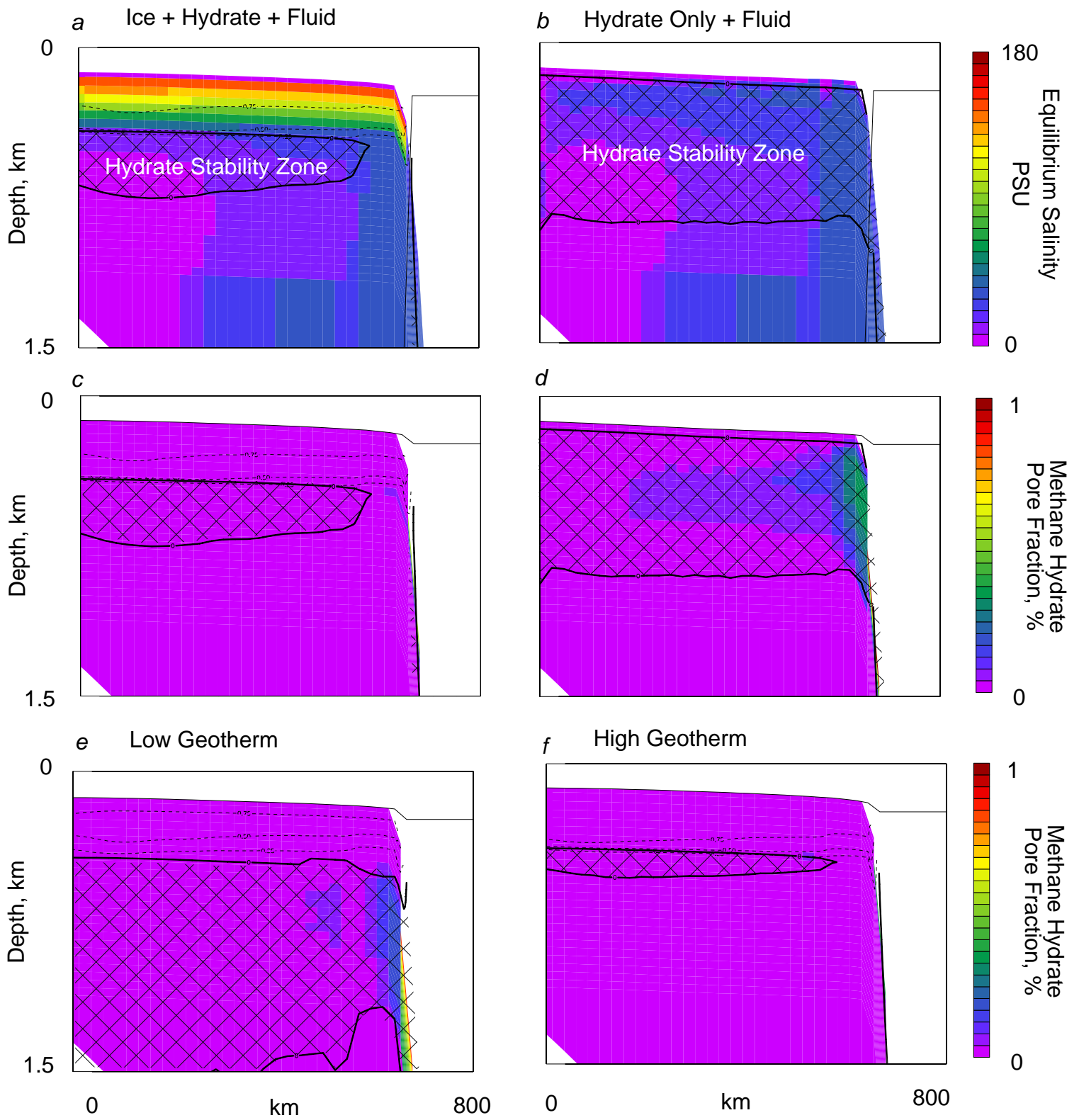


Figure 8

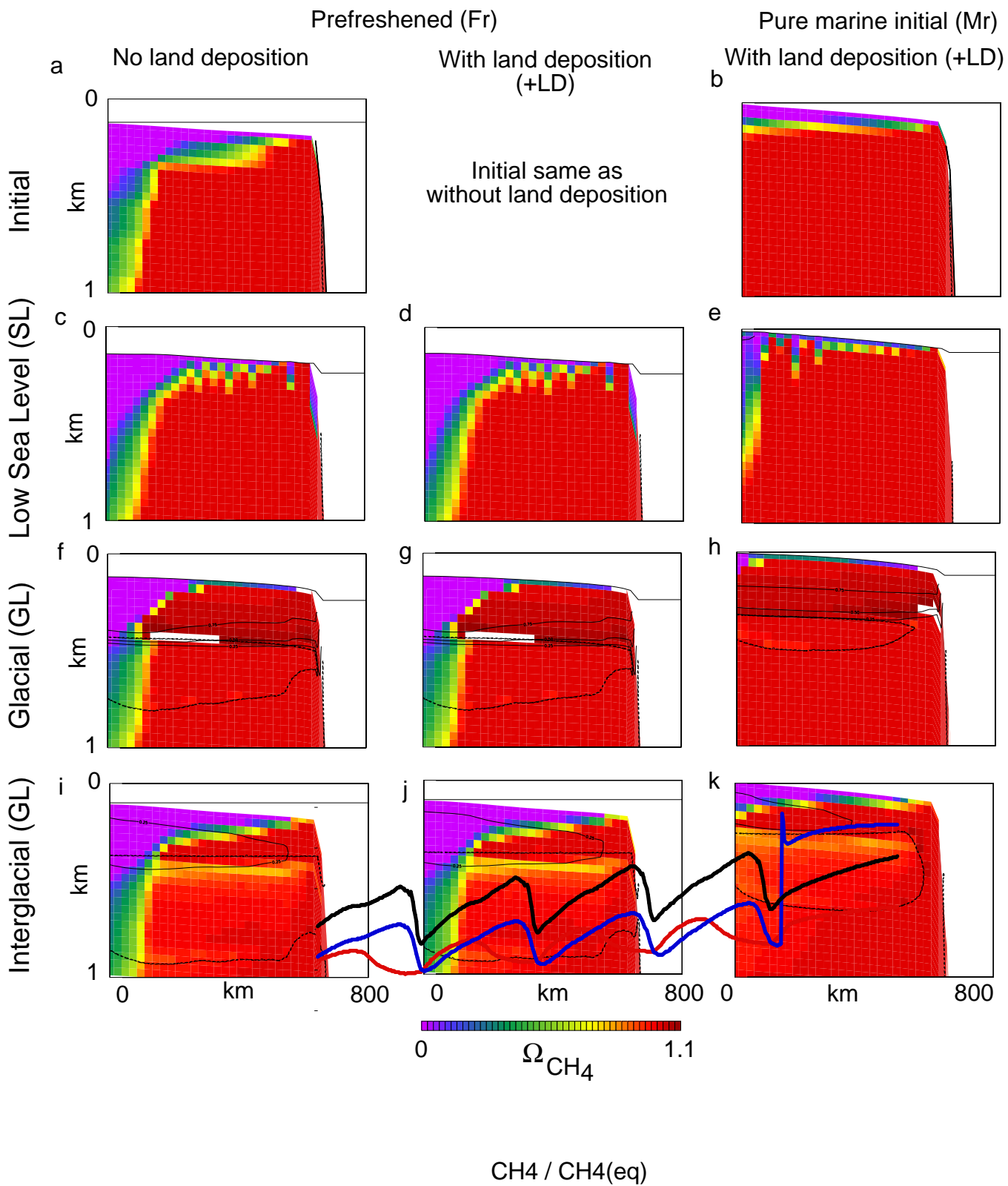


Figure 9

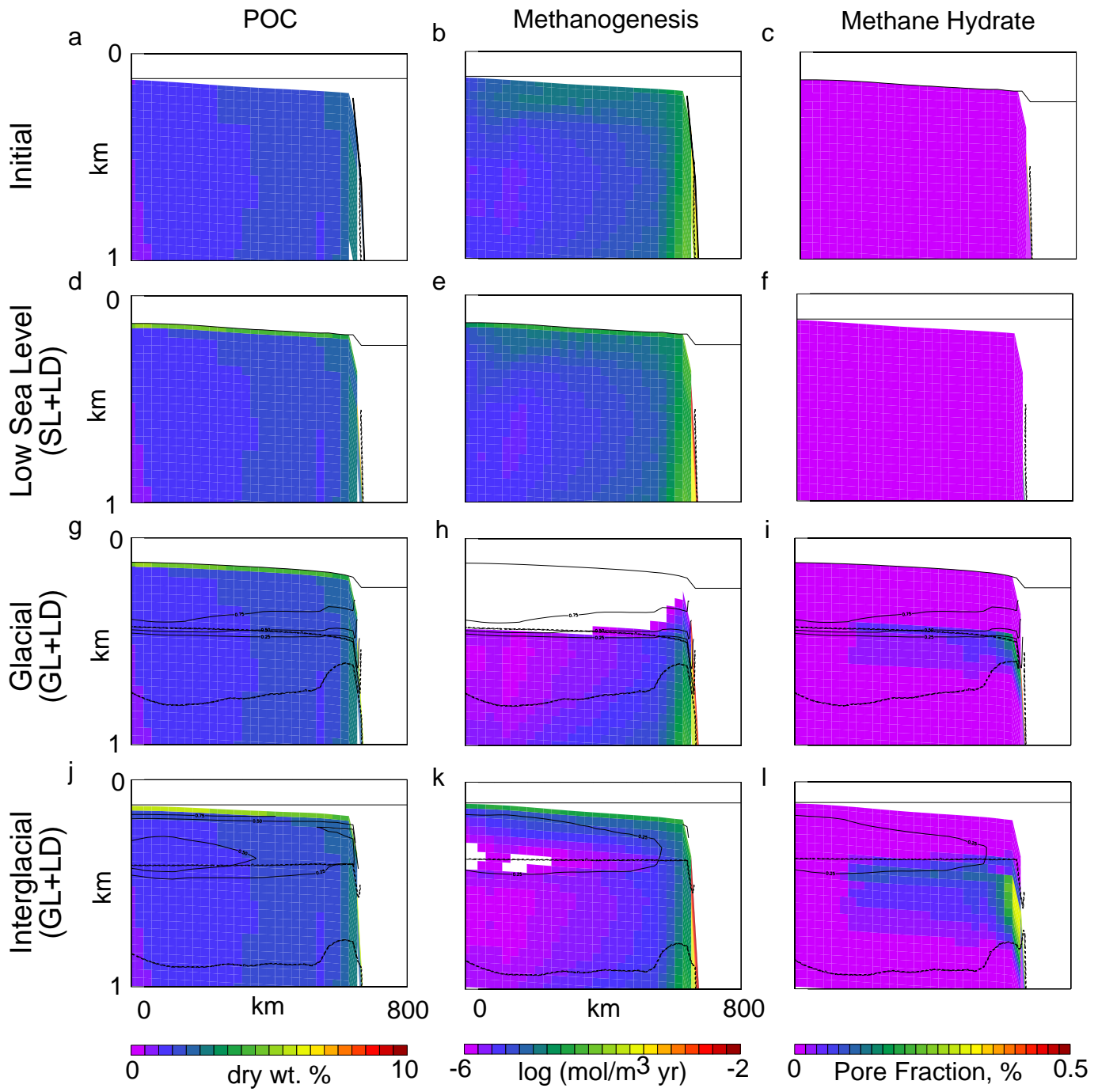


Figure 10

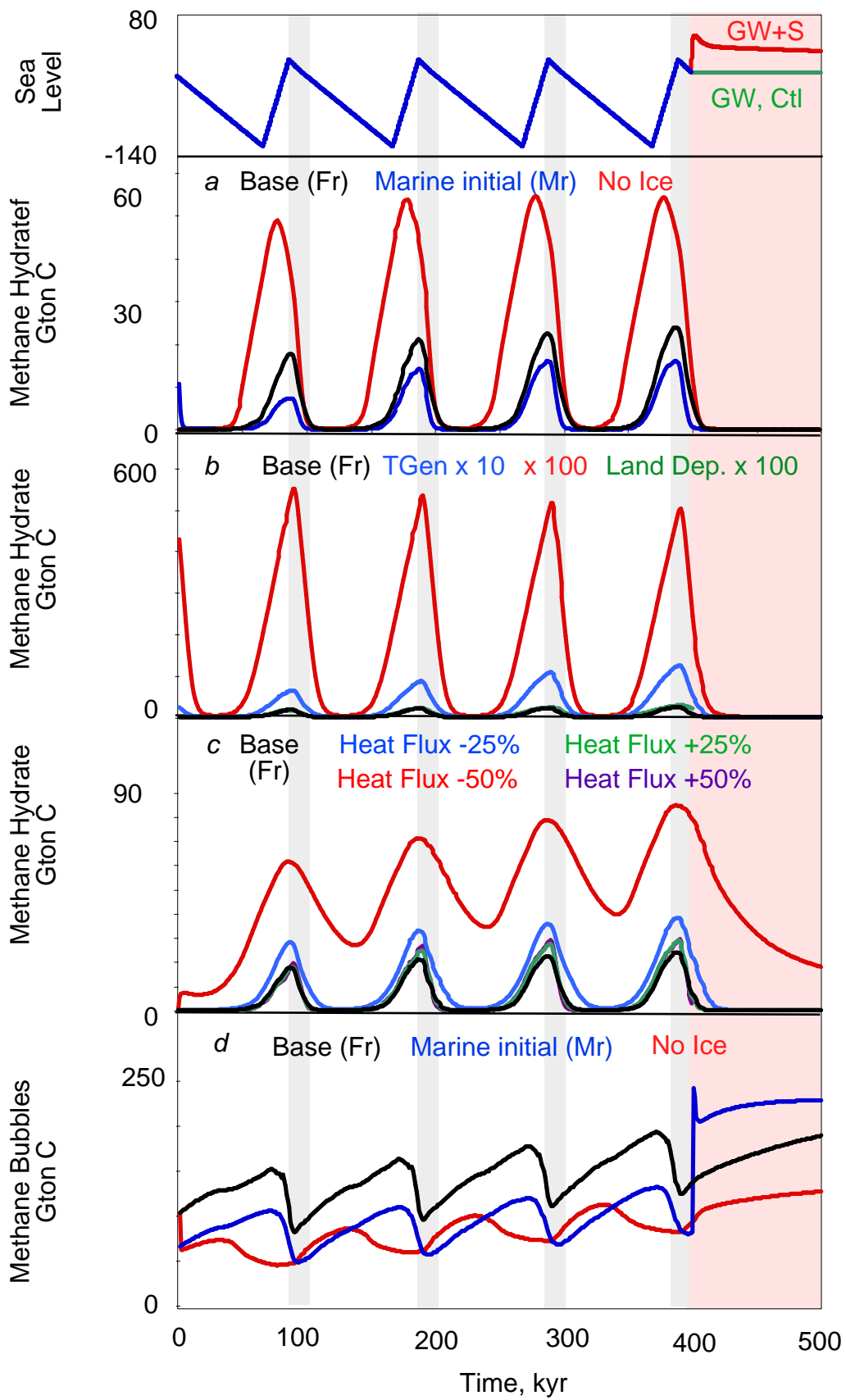


Figure 11

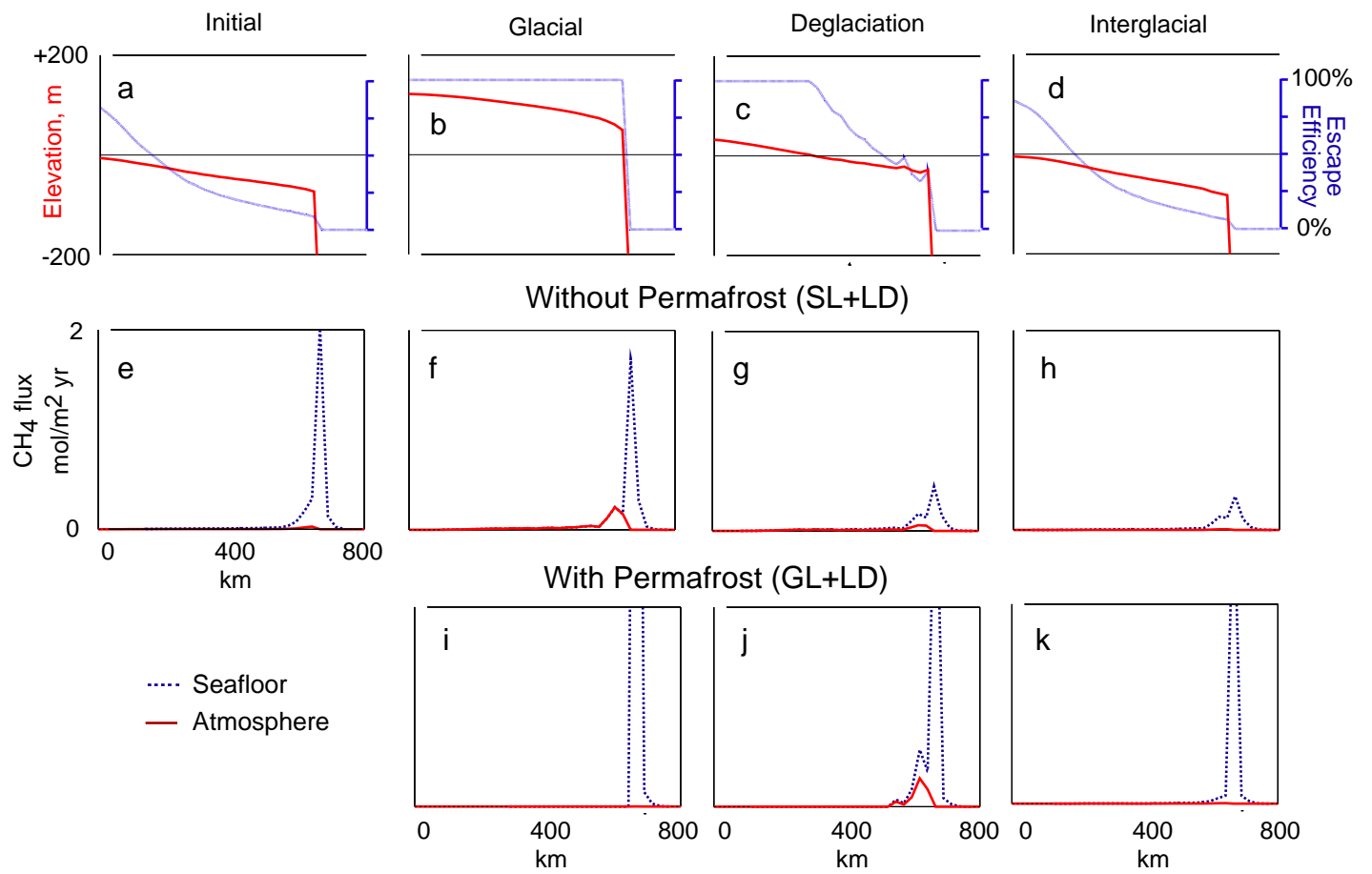


Figure 12

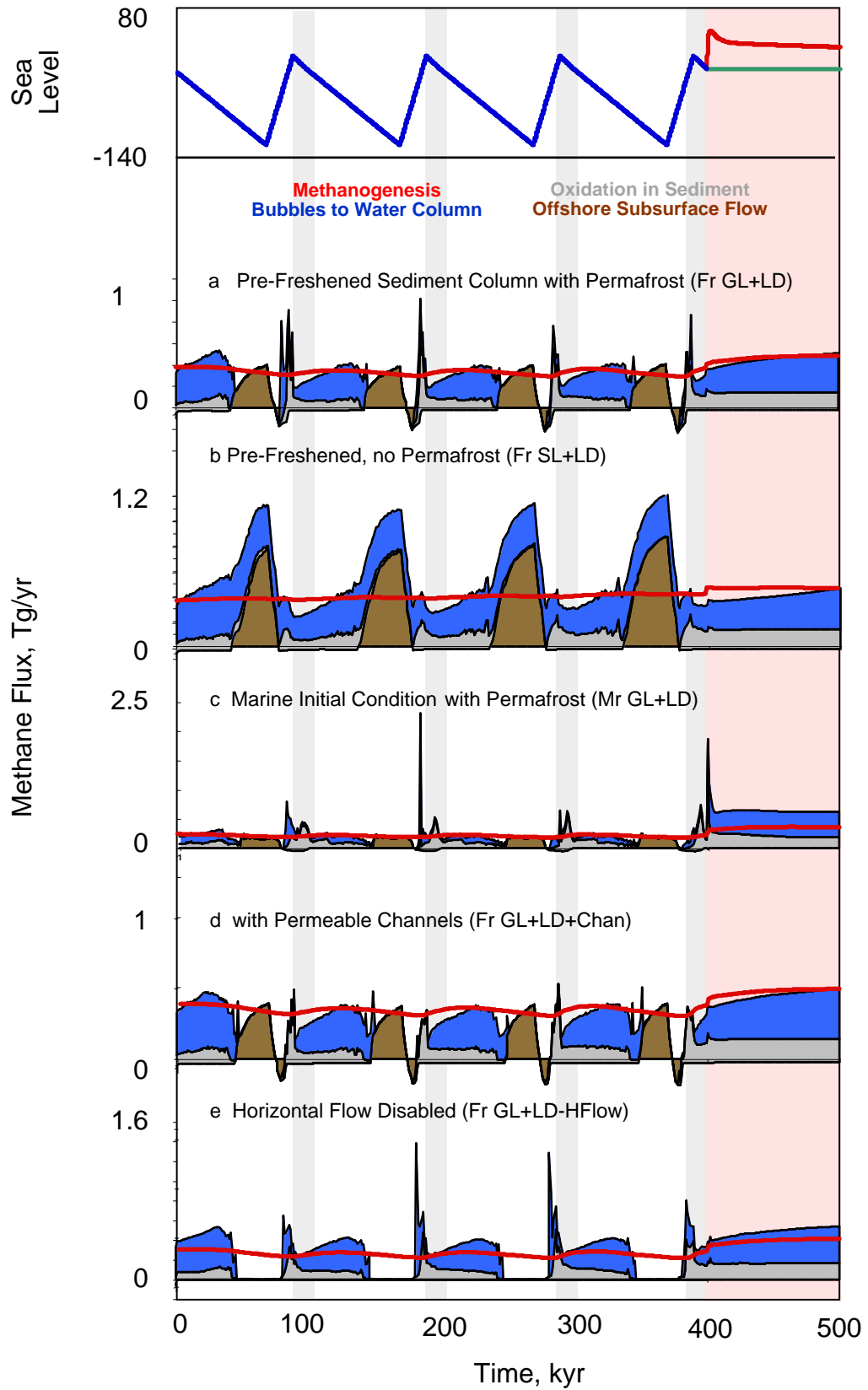


Figure 13

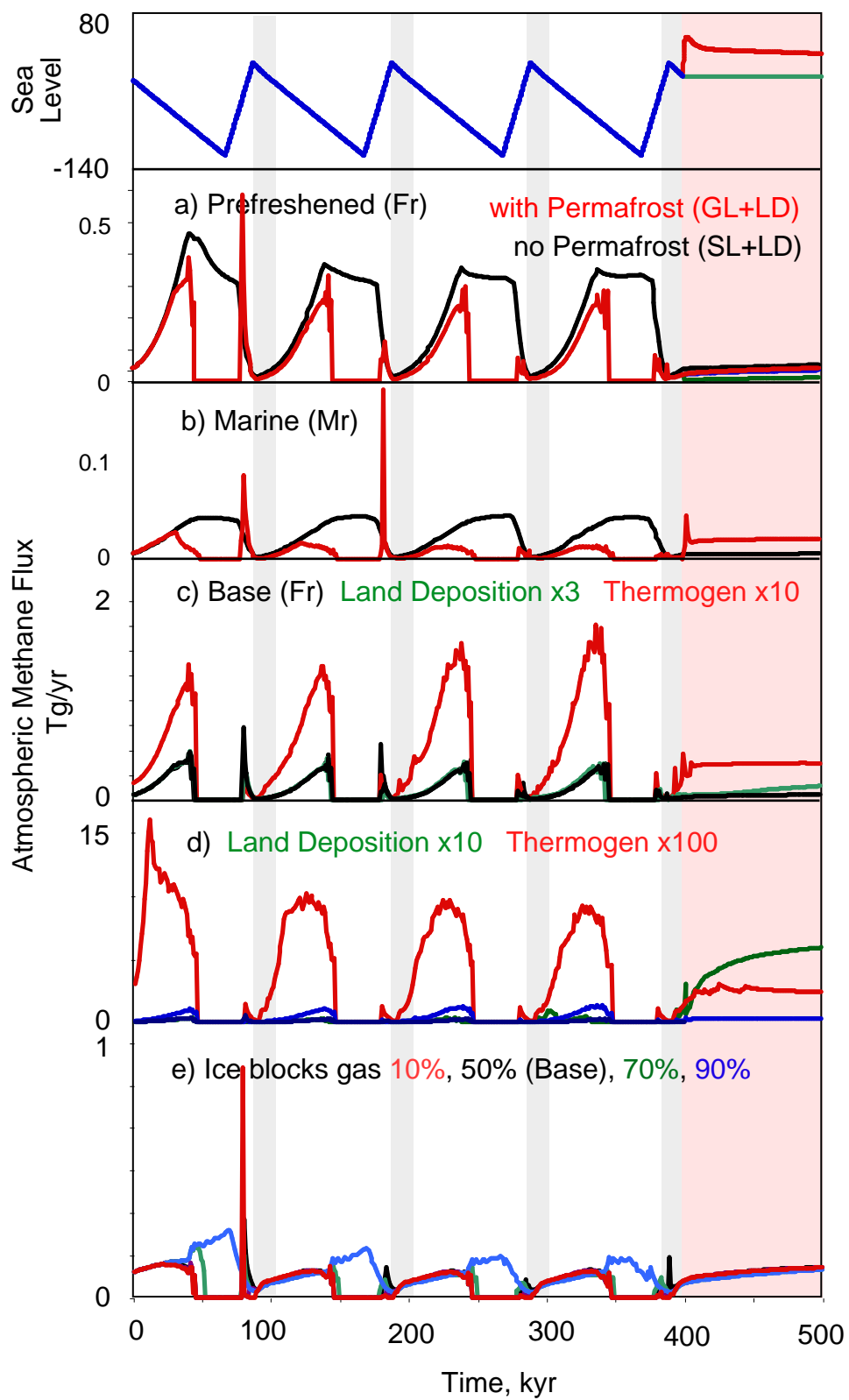


Figure 14

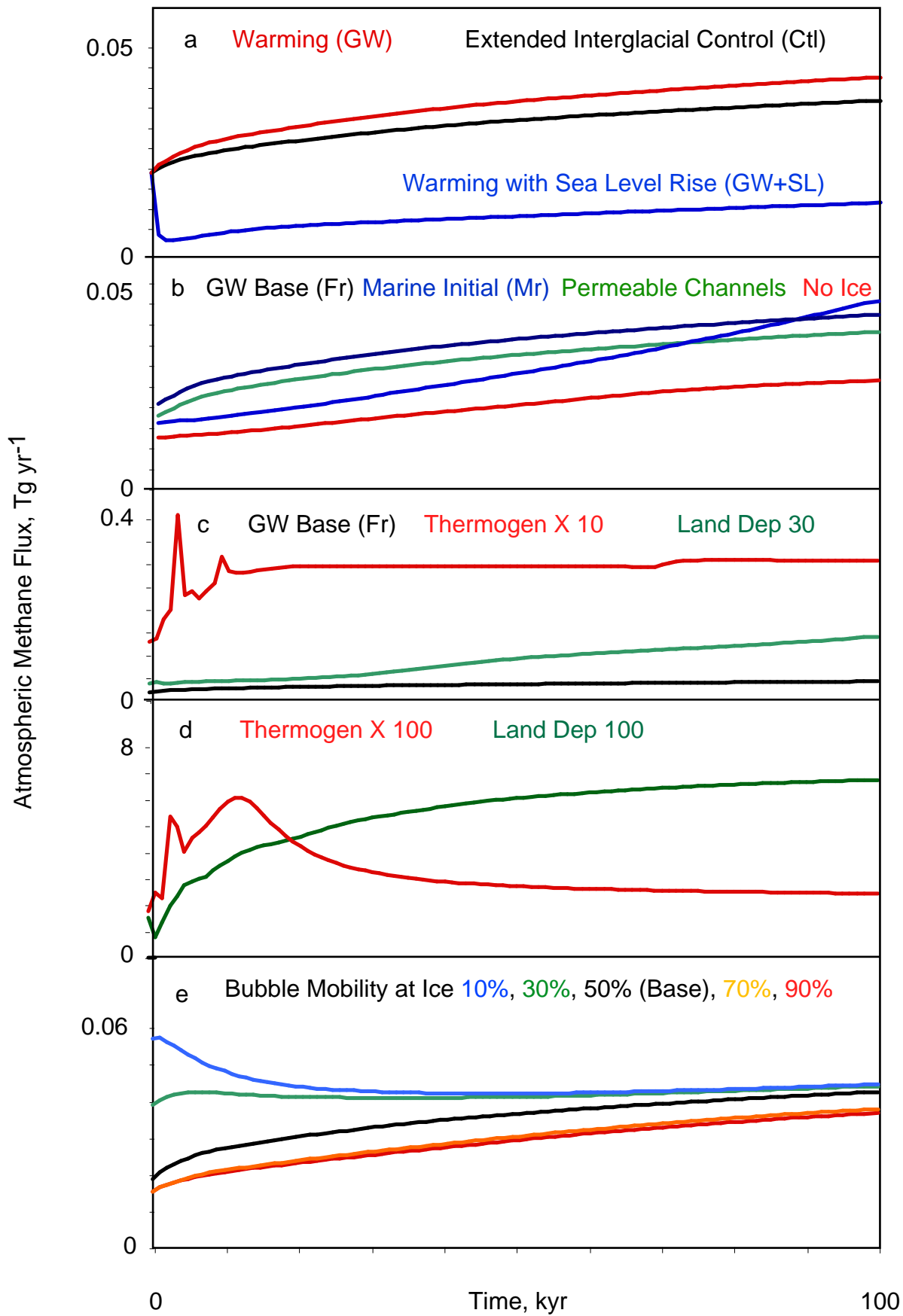
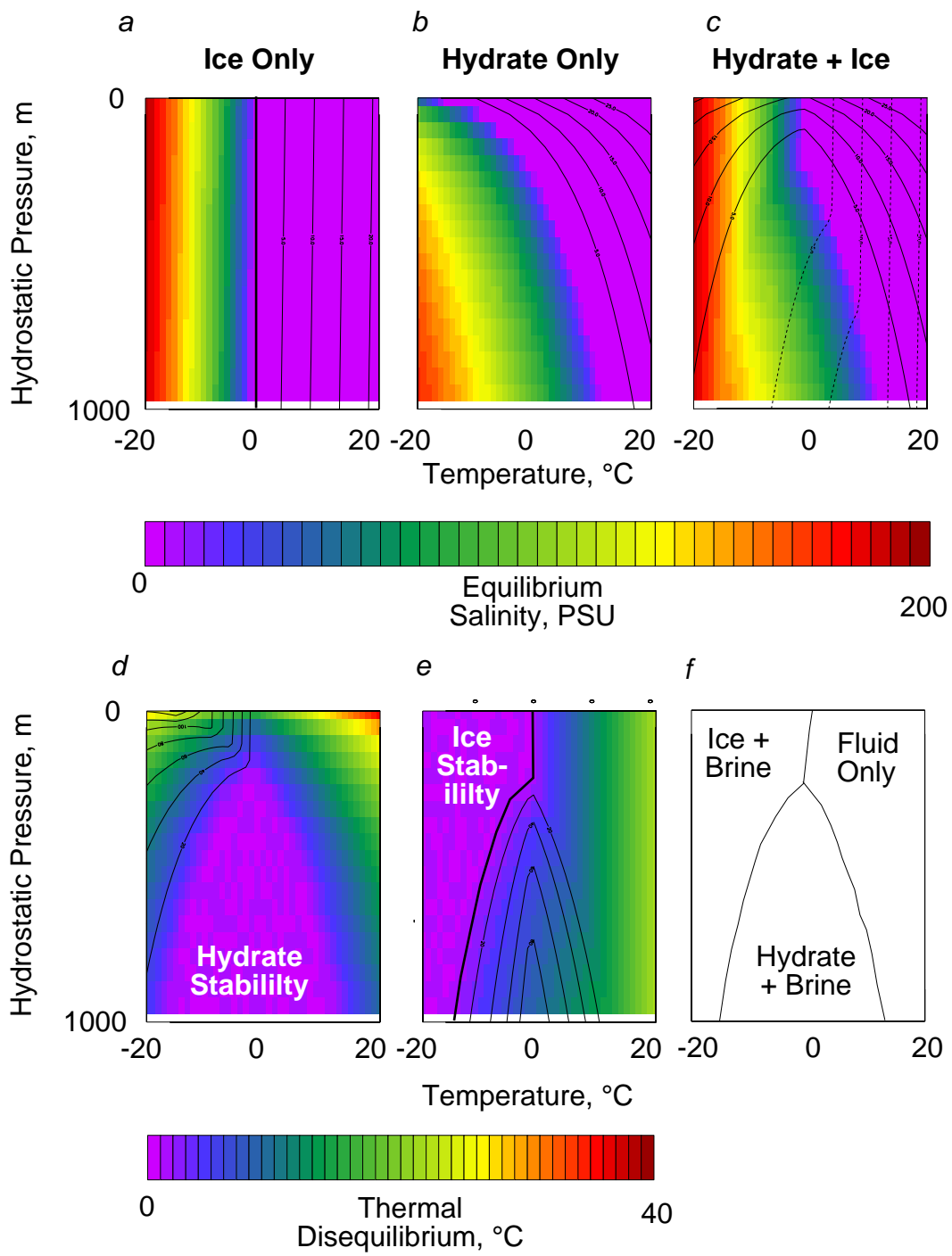
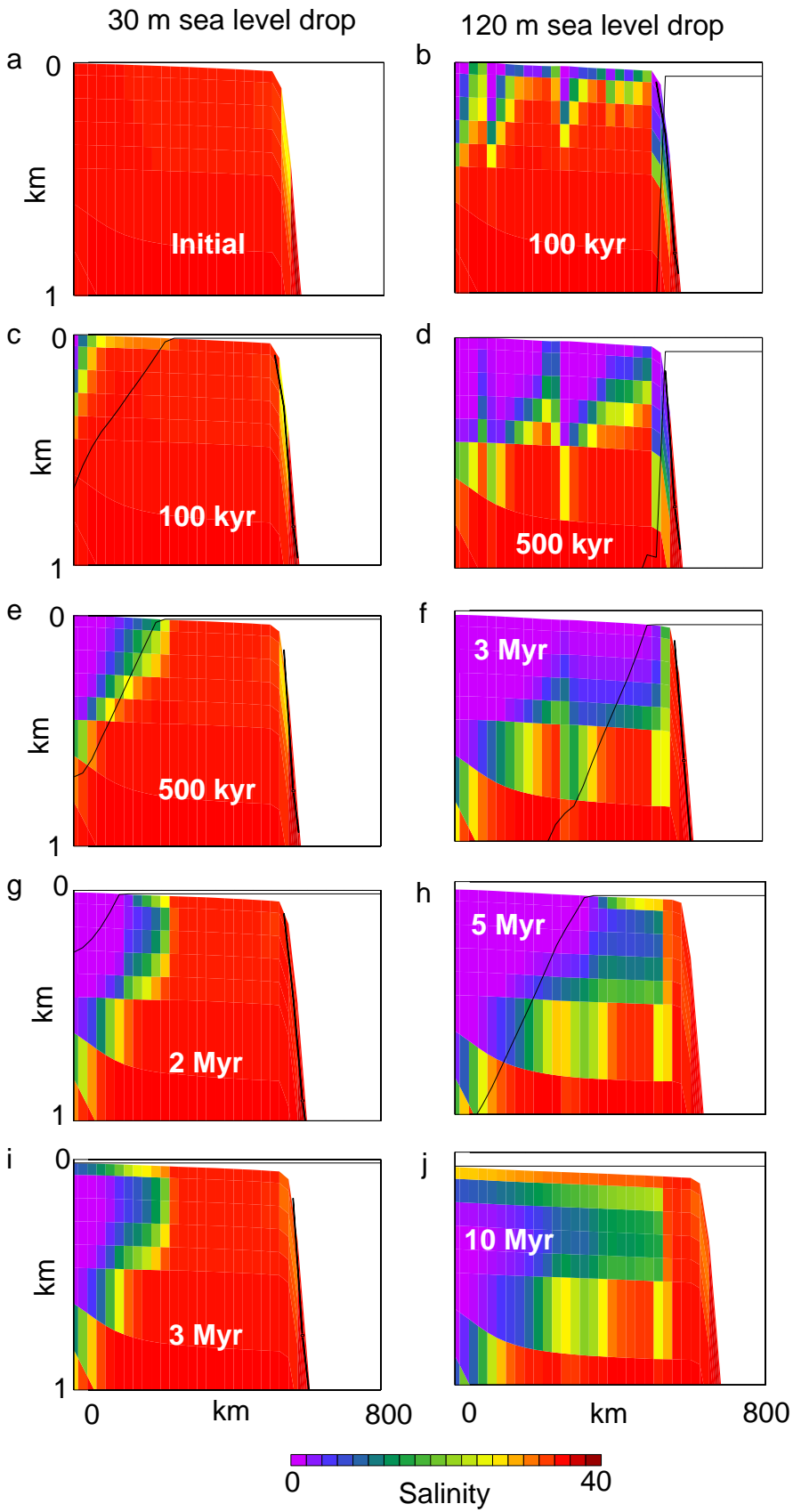


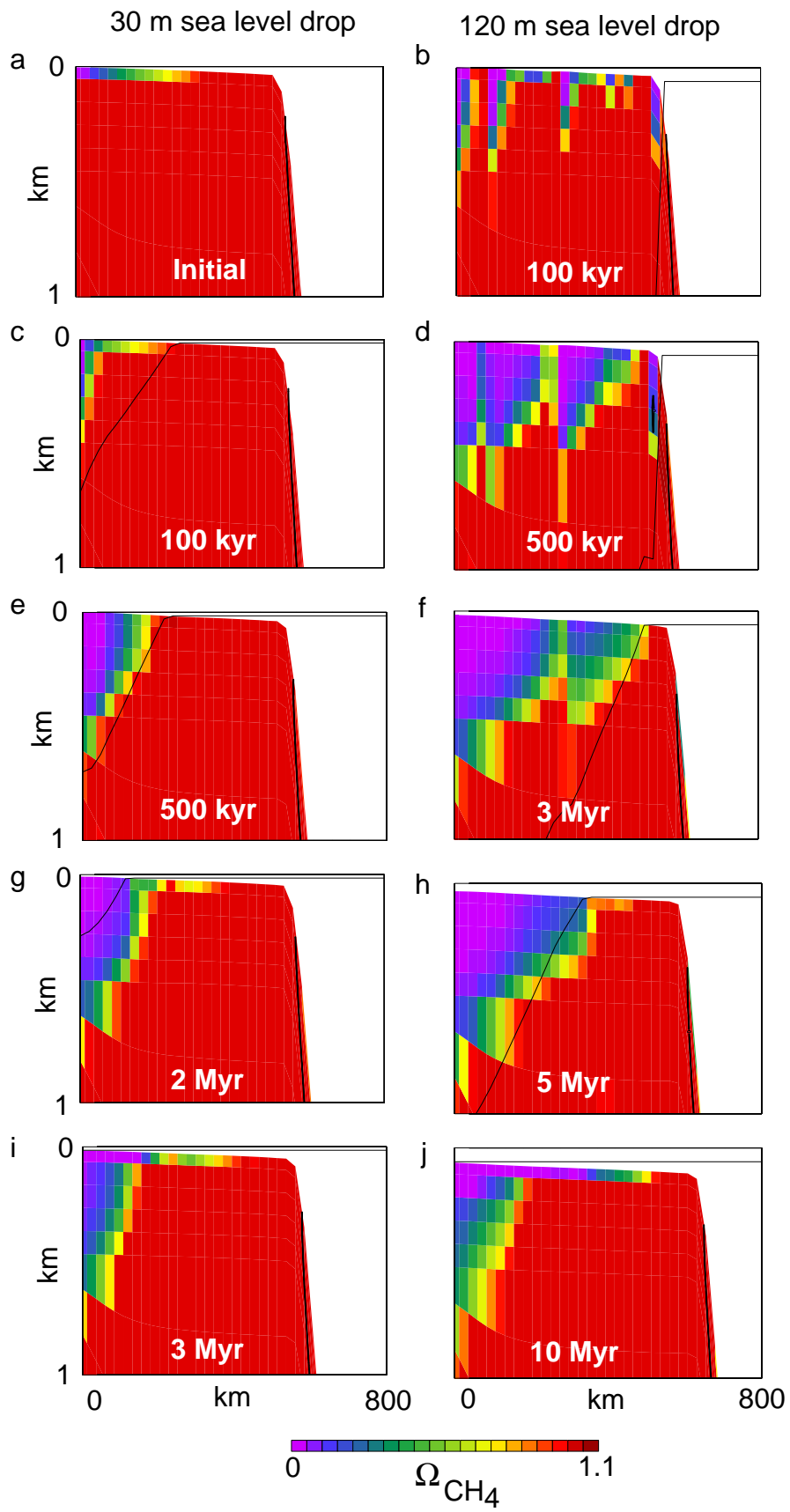
Figure 15



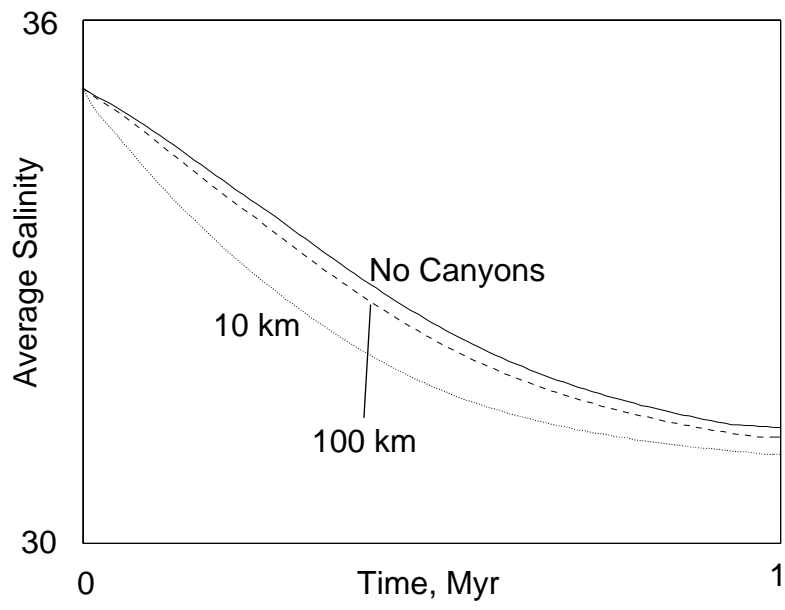
Supplemental Figure 1



Supplemental Figure 2



Supplemental Figure 3



Supplemental Figure 4